Department of Physics and Astronomy

University of Heidelberg

Master thesis

in Physics

submitted by

Alexander Hesse

born in Werl

2019

A NV center based

magnetic field stabilization

for atomic physics experiments

This Master thesis has been carried out by Alexander Hesse

at the

Kirchhoff-Institute for Physics

under the supervision of

Prof. Fred Jendrzejewski

Eine NV-Zentrum basierte Magnetfeldstabilisierung für Atomphysikexperimente

In Atomphysikexperimenten erlaubt einem das Regeln der Magnetfelder, Spindynamik zwischen den Atomen zu erzeugen, oder ihre Wechselwirkung frei einzustellen. Dies macht stabile Magnetfelder sehr erstrebenswert, aber leider existiert kein kommerzieller Magnetfeldsensor, der Felder, die größer als 20 Gauss sind, mit hinreichender Genauigkeit messen kann, um in einer Regelschleife verwendet zu werden.
In dieser Arbeit stelle ich eine Magnetfeldstabilisierung vor, die als Magnetfeldsensor NV Zentren verwendet. Durch die Datenauswertung auf dem FPGA eines RedPitayas wird der Aufbau kompakt gehalten, und wenige Bauteile werden benötigt, um die Zeemanverschiebungen in den NV Zentren zu spektroskopieren, und so das Magnetfeld zu bestimmen.
Die gemessenen Magnetfeldschwankungen können in unserem Aufbau auf 1.1 mG hinuntergeregelt werden, was einen Faktor 2.5 über dem Schrotrauschen unserer Sensoren liegt. Durch das Verwenden einer präzisen Frequenzquelle können mittlere Stabilitäten von 300 ppb auf einer Zeitskala von 30 Minuten erreicht werden.

A NV center based magnetic field stabilization for atomic physics experiments

In atomic physics experiments, setting the magnetic field strength allows one to create spin dynamics between atoms, or to tune the interaction between them. This makes stable magnetic fields desirable, but unfortunately no commercially available sensor can measure magnetic fields past 20 Gauss with high enough precision to be used in a feedback loop.
In this thesis, I present a magnetic field stabilization based on NV centers as a sensor. The setup is kept compact by moving the data treatment to a RedPitaya's FPGA, and few components are needed to build the setup for performing spectroscopy on the NV center's Zeeman shift.
The measured magnetic field noise in our setup can be regulated down to 1.1 mG over the control loop bandwidth of 1 kHz, which is about 2.5 times above the shot noise limit of our sensors. Using a precise frequency source the long term stability reaches 300 ppb on average over 30 minutes.

Shine bright like a diamond.

RIHANNA

Contents

1 Introduction

This thesis was motivated by ultracold atom experiments, in this case specifically by a mixture of ^{23}Na and ^{39}K or ^{23}Na and ^{40}K. Cold atom experiments form a convenient platform for the study of many body phenomena, and allow for the quantum simulation of processes and effects known from other fields of physics:

One fairly straightforward phenomenon to study when working with both a bosonic ^{23}Na and a fermionic ^{40}K species is the Kondo effect (as illustrated in figure 1.1): The Kondo model describes the behaviour of the conduction electrons in a metal in presence of a magnetic impurity. While, at high temperatures, this impurity is shielded off by the so-called Kondo cloud, and at low temperatures the spin of this impurity forms a singlet state with the spin of one of the conduction electrons, at intermediate temperatures - near the Kondo temperature - the spin of the impurity can interact with the neighbouring electrons' spins.

This effect could be studied by placing an impurity (a single sodium atom) in a bath of fermions (potassium 40 atoms) and letting the spins of the two species interact for different initial conditions (as proposed in [1]).

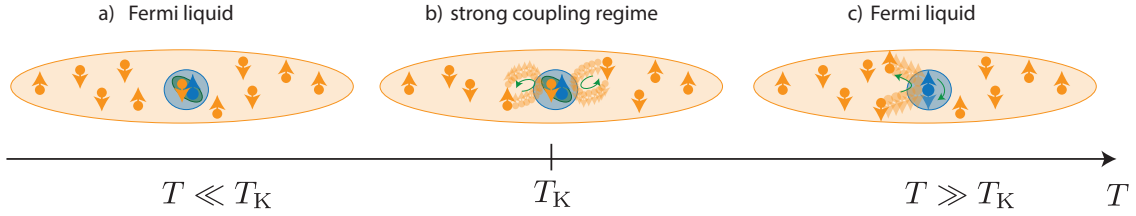

Figure 1.1: Illustration of the Kondo effect: An impurity is located in a fermionic bath (e.g. a metal). While for low temperatures **a)** the impurity forms a singlet state with a neighbouring atom, and for high temperatures **c)** the impurity is screened off by the Kondo screening cloud, near the Kondo temperature T_K interactions between the spin of the impurity and the fermionic bath are possible, as illustrated in **b)**. Figure taken from [1].

Another direction to take these experiments to is the simulation of high energy physics [2, 3]: As illustrated in figure 1.2, we can use the bosonic and the fermionic species to act as the electromagnetic field and matter, with one spin state denoting existing matter, and the other one vacuum. By letting the spins of the bosons and fermions interact, one can now for instance create a particle using energy from the electromagnetic field, and study Schwinger pair production [4].

In both experiments proposed, changing collisions between the two different species

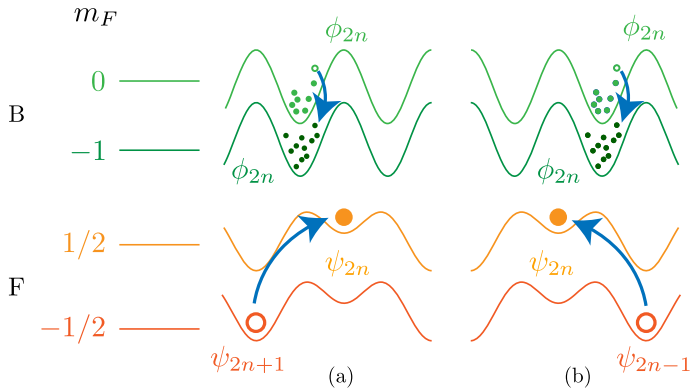

Figure 1.2: Proposed scheme for simulation of quantum electrodynamics: A bosonic bath acts as the electromagnetic field, while single fermions placed in the same optical superlattice represent matter. Interaction between those two can now be simulated using spin changing interactions. Figure taken from [2].

is the driving dynamic. In the following chapter, I will talk about the interaction of atoms with magnetic fields, and will show that, in order to observe spin changing collisions, extremely stable magnetic fields are needed. After that, I will describe how the magnetic fields can be stabilized for such experiments, and why such stable magnetic fields could not be achieved previously.

1.1 Atoms in magnetic fields

In the experiments described in the previous section the interest lies in the spin dynamics for alkali metals. This simplifies the calculation the energy levels significantly, as the analytical Breit-Rabi equation [5] can be used, which covers both the Zeeman- and the Paschen-Back regime:

$$E(B) = -\frac{a_{hfs}}{4} + g_i m_f \mu_B B \pm \frac{a_{hfs}(I + 1/2)}{2} \cdot \sqrt{1 + \frac{2x \cdot m_f}{I + 1/2} + x^2} \tag{1.1}$$

Where a_{hfs} is the magnetic dipole constant, g_i the nuclear spin factor, g_j the electron spin g-factor and μ_B the Bohr magneton. Additionally, x is used to substitute:

$$x = \frac{g_j - g_i}{a_{hfs}(I + 1/2)} \mu_B B \tag{1.2}$$

With this I calculated the energy levels for the three species of interest, as shown in figure 1.3.

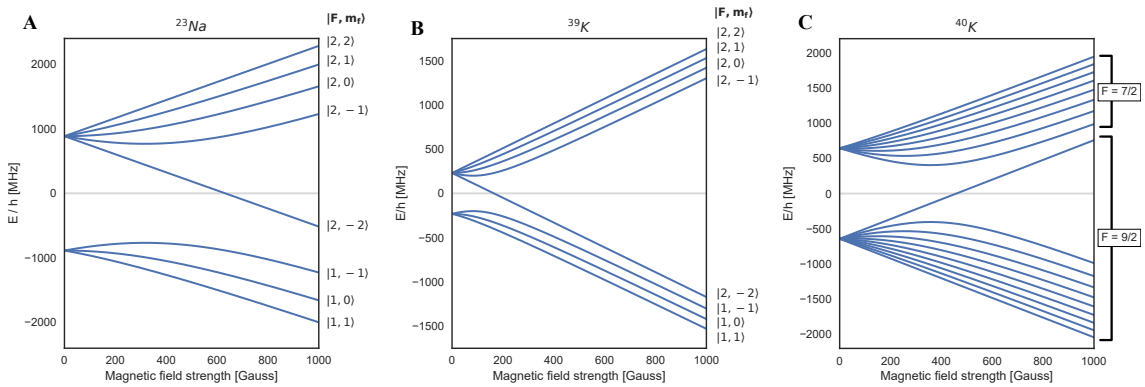

Figure 1.3: Breit-Rabi diagrams for **(A)** ^{23}Na, **(B)** ^{39}K as well as **(C)** ^{40}K. The low field quantum numbers $|F, m_f\rangle$ are used to label the different states, except for ^{40}K, where, due to the vast number of states, only F is given.

1.2 Spin changing collisions

The general idea behind spin changing collisions is a fairly simple one: We want two atoms (in our case, atoms of two different species) to hit each other, and to exchange spin while doing so, as illustrated in figure 1.4. For this process to happen without additional energy being converted into heat, the spacing between the two energy levels of interest $\Delta E_{Na} - \Delta E_K$ has to be equal for both atoms.

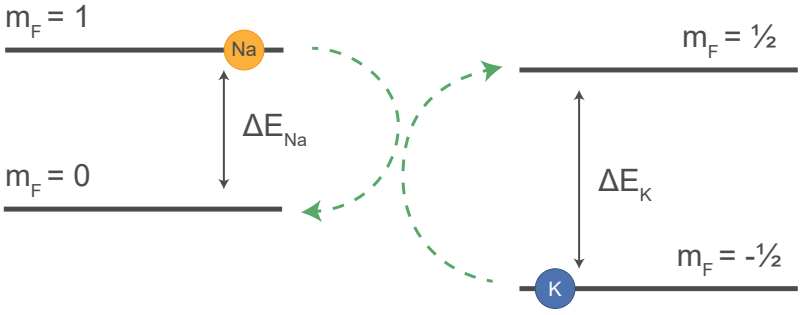

Figure 1.4: Illustration for spin changing collisions between ^{23}Na and ^{40}K.

Initially, this might sound trivial, as of course the energy spacings between the spin states are always equal for no magnetic field applied. However, there can also be a second point for this to happen, when the quadratic Zeeman shift becomes larger than the linear one. Finding now all possible scenarios for this is just a matter of combining the previously calculated energy levels, under consideration of spin conservation.

For spin changing collisions between ^{39}K and ^{23}Na two possible realizations have been found this way, illustrated in figure 1.5. Both of these scenarios are close to 1 Gauss. The magnetic field stability needed to observe spin changing collisions between the sublevels is related to the slope of the derivative of the energy difference at the position of the zero crossing. For both cases, it is about 1.1 kHz, so there is

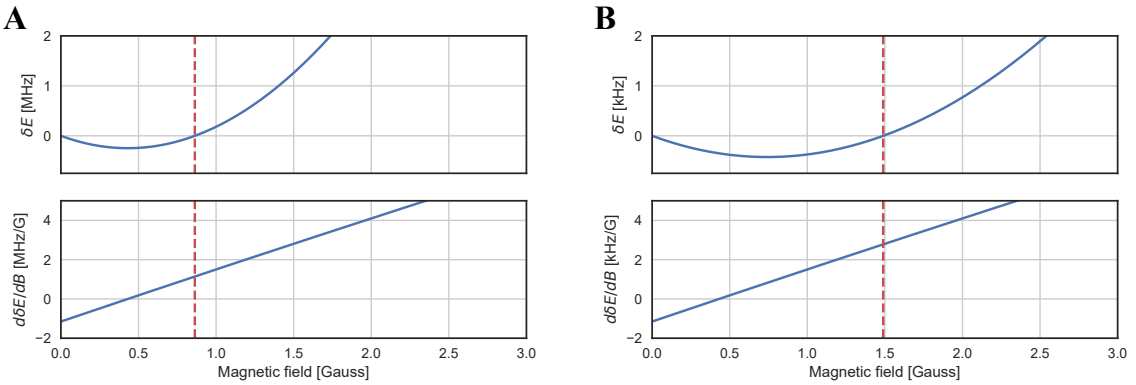

Figure 1.5: **(A)** Spin changing collisions for the $|m_f^{39K} = -1, m_f^{23Na} = 0\rangle \rightarrow |m_f^{39K} = 0, m_f^{23Na} = -1\rangle$ transition. A resonance is present at 1.5 Gauss, with a slope of 1.1 kHz/Gauss. **(B)** Same as in **(A)**, but for the $|m_f^{39K} = 1, m_f^{23Na} = 1\rangle \rightarrow |m_f^{39K} = 0, m_f^{23Na} = 0\rangle$ transition. The energy difference is zero at 0.86 Gauss, with a slope of 1.1 kHz/Gauss.

no intrinsic benefit in choosing one realisation over the other.

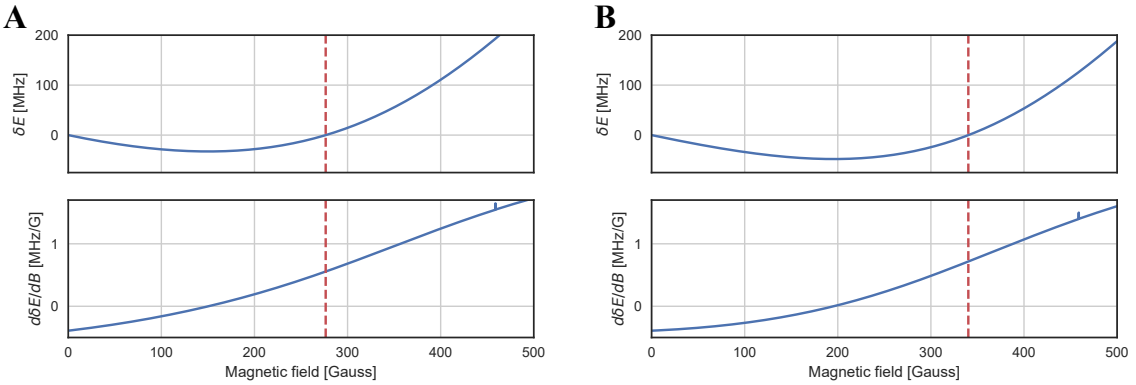

Figure 1.6: **(A)** Spin changing collisions for the $|m_f^{40K} = -7/2, m_f^{23Na} = 1\rangle \rightarrow |m_f^{40K} = -5/2, m_f^{23Na} = 0\rangle$ transition. A resonance is present at 277 Gauss, with a slope of 0.55 MHz/Gauss. **(B)** Same as in **(A)**, but for the $|m_f^{40K} = -7/2, m_f^{23Na} = 0\rangle \rightarrow |m_f^{40K} = -5/2, m_f^{23Na} = -1\rangle$ transition. The energy difference is zero at 340 Gauss, with a slope of 0.72 MHz/Gauss. Notice how both magnetic field scale as well as energy scale changed significantly, as compared to figure 1.5!

When determining the magnetic field strengths needed to see spin changing collisions between ^{23}Na and ^{40}K however, much larger fields are needed: Here, two realizations can be found, and both occur at magnetic field strengths close to 300 Gauss, with slopes of about 0.6 MHz/Gauss - not only are the magnetic field strengths needed much larger, but also the stability needs to be about a factor 500 better! This poses a challenge on current experimental setups, and is hard to realize.

1.3 Feshbach resonances

Another important tool in atomic physics are magnetic Feshbach resonances [6]. For ultracold atoms, the de-Broglie wavelength typically is much larger than the effective van-der-Waals potential between them, concealing its complex structure, and allowing scattering processes to be described by a single parameter, the s-wave scattering length a. This scattering length can be thought of as the radius of a classical sphere, the larger it becomes, the more repulsive the interaction between the two atoms becomes. However, also negative scattering lengths are possible, in which case the interaction between the atoms becomes attractive.

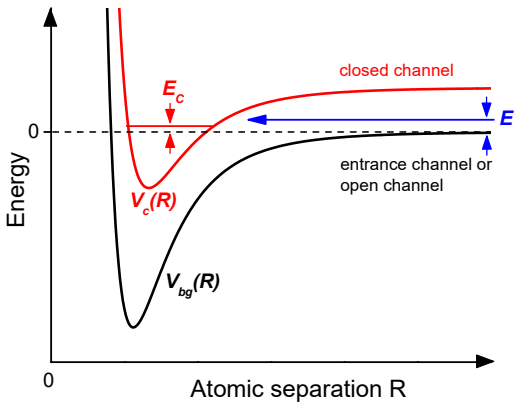

Figure 1.7: Illustration of the two channel model for a Feshbach resonance. Taken from [6].

These properties lead to the formation of a Feshbach resonance in systems similar to the one illustrated in figure 1.7. The black potential $V_{bg}(R)$, or the so called open channel, represents the energy of two unbound particles. However, also a closed channel $V_c(R)$ exists, containing a bound state at energy E_c between the two atoms.

By making use of the Zeeman shift, we can now shift the energy E_c by tuning the magnetic field. This way a Feshbach resonance between E_c and the energy of the two atoms E can be formed. Near this resonance, the scattering in dependence of the magnetic field is given by:

$$a(B) = a_{bg}\left(1 - \frac{\Delta}{B - B_0}\right) \tag{1.3}$$

Here a_{bg} is the background scattering length associated with the open channel potential V_{bg}, B_0 is the magnetic field, at which the scattering length diverges, and Δ is the width of the resonance.

This ability to tune the scattering length between atoms enables the study of a plethora of different effects: By tuning the magnetic field across a Feshbach resonance, molecules can be associated from single atoms [7, 8]. Molecules created from fermions can then form a Bose-Einstein condensate [9, 10]. Now another possibility is the study of the BEC-BCS crossover in fermionic quantum gases [11, 12, 13]. For bosonic quantum gases, the study of bright solitons [14, 15], and, more recently, quantum liquid droplets [16, 17] were made possible.

1.4 Magnetic field stabilization

In the previous sections we have seen that very stable magnetic fields are key in order to observe spin dynamics in our system - however, magnetic field noise sources are present at all times, the power line current at 50 Hz alone already generates magnetic fields in the order of several mG. This makes active magnetic field stabilizations necessary, and with such stabilizations it has already been possible in the past to observe spin changing collisions [18, 19, 20].

Typically, fluxgate sensors are employed for such applications, as they offer high high resolutions of lower than 100 $\frac{\text{nG}}{\sqrt{\text{Hz}}}$ [21]. Unfortunately, their measurement range is typically limited to up to 10 Gauss, which would allow us to study spin changing collisions between ^{23}Na and ^{39}K, but the magnetic fields needed for spin changing collisions between ^{23}Na and ^{40}K at 300 Gauss are far out of reach.

The other commonly available magnetometer, Hall sensors, do cover a large magnetic field range up to about 1000 Gauss, but lack precision - a resolution in the $\frac{\text{mG}}{\sqrt{\text{Hz}}}$ range is generally considered very good [22].

This shows up the need for alternative sensors, which allow for the precise mea-

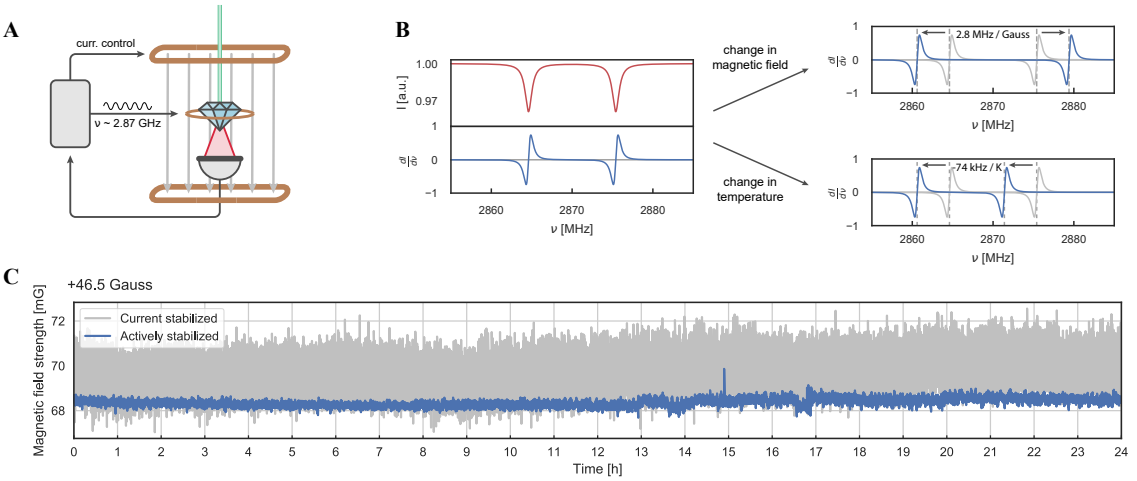

Figure 1.8: (A) Experimental setup: The NV center are positioned in a magnetic field generated by a pair of Helmholtz coils. They are excited by a green laser, and the red fluorescence collected on a photodiode is fed into a control circuit, which also controls the microwave signal applied to a wire loop around the NV centers. From the fluorescence a magnetic field reading is extracted, and used to regulate the current through the coil pair. **(B)** Shift of the two transitions $m_s = 0 \rightarrow m_s = -1$ and $m_s = 0 \rightarrow m_s = 1$ with temperature and magnetic field as visible in the fluorescence signal. **(C)** Comparison of the magnetic field reading on an independent second sensor for - in grey - just a current stabilization on the coil current to - in blue - the coil current being regulated to the NV center's reading.

surement of larger magnetic fields than possible with a fluxgate sensor. Ideally, such a sensor would cover a range of several hundreds of Gauss with a precision better than 30 $\frac{\mu\mathrm{G}}{\sqrt{\mathrm{Hz}}}$, to allow for the stabilization of magnetic fields to better than a mG over a 1 kHz bandwidth.

In recent years, many magnetic field sensors based on quantum mechanics were developed: Superconducting quantum interference devices (SQUIDs) have demonstrated sensitivites well below 1 $\frac{\mathrm{nG}}{\sqrt{\mathrm{Hz}}}$ [23, 24]. Another new and precise sensor are atomic clouds, also yielding precisions below 1 $\frac{\mathrm{nG}}{\sqrt{\mathrm{Hz}}}$ [25, 26].

However, both these methods are relatively complex to realize, and the size of the setup is fairly big. For our application, it is important for the sensor to be as close to the atoms as possible in order to ensure that the magnetic field detected by the sensor is identical to the one experienced by the atoms.

Another quantum sensor, that has emerged in recent years is the nitrogen-vacancy (NV) center in diamond. Yielding precisions of a few $\frac{\mathrm{nG}}{\sqrt{\mathrm{Hz}}}$ [27], its strength lies in the sensing of very localized magnetic fields in confined spaces [28, 29, 30].

In the following chapters, I will describe the design of a magnetic field stabilization based on NV centers, stabilizing our magnetic field to 1.1 mG RMS over the control loop's bandwidth, with 300 ppb noise on a 30 minute time scale:

- In the next chapter, the structure and the spectrum of NV centers will be discussed. From this, a simple magnetometry scheme can be derived.
- After that, the experimental setup we used will be discussed, already keeping in mind the sensor noise. Ways of reducing noise in the magnetic field signal will be presented.
- The fourth chapter deals with NV center magnetometry. As the design of the experimental setup was an iterative process, many noise measurements had to be done in order to get a precise sensor.
- Then the feedback loop is closed, and the performance of our magnetic field stabilization is characterized by performing several measurements of different length. The main limitations for AC and DC performance are determined, and ways of reducing them are discussed.
- In the end, a way of implementing the magnetic field stabilization into a running atomic physics experiment will be presented. Possible experiments for combining NV centers with atomic physics are proposed.

2 The nitrogen vacancy center in diamond

The nitrogen vacancy (NV) center in diamond has over the last decades emerged as a compact and easy to use quantum system [31]. It can be used to measure magnetic fields, temperature, lattice strain as well as electric field, with its main benefit being the small size, allowing to measure in very confined spaces [28]. By coupling it to neighbouring ^{13}C atoms in a diamond lattice, coherence times over one second can be achieved [32], making it a suitable system for quantum information processing [33].

Our main interest lies in the use of NV centers as a magnetic field sensor, with the plan to stabilize the magnetic fields in our experiment at large magnetic field values. Fairly simple measurement schemes are possible, as explained in the following chapter.

2.1 Lattice structure

Much about the NV center's behaviour can be understood from its lattice structure, so that this section will give a brief introduction into the NV center's structure, also illustrated in figure 2.1:

The NV (standing for nitrogen vacancy) center one of many possible defects in a diamond lattice. It consists of both a nitrogen atom, as well as a vacancy occupying a neighbouring lattice site.

However, the electronic structure of this configuration is very different from that of a regular diamond lattice: While nitrogen actually has a valence electron more than carbon, the vacancy obviously contains no electrons at all, and therefore cannot bond to any of the electrons of the neighbouring atoms.

As nitrogen has one valence electron more than carbon we are here left with two unbound electrons - these electrons will form a lone pair, as illustrated in figure 2.1 (C). Also, two of the three electrons of the carbon atoms will form a quasi covalent bond, leaving only one electron unpaired. This defect is known as the NV^0 center, containing a spin $^1/_2$ system.

Interesting properties arise, when in addition to the electron at the vacancy, an additional electron is donated, e.g. by another nitrogen atom nearby. These two

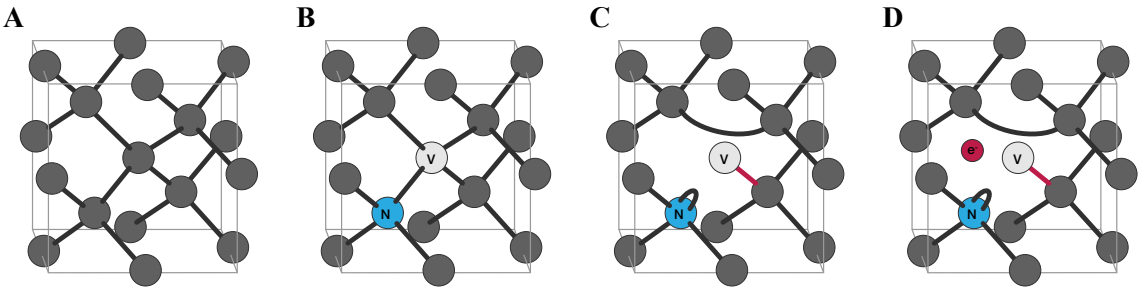

Figure 2.1: Derivation of the lattice structure of the NV center: **(A)** Lattice structure of diamond. **(B)** In this lattice, one carbon atom is replaced with a nitrogen atom, and a neighbouring lattice site is left as a vacancy. Notice, how the electronic connections of diamond cannot stay the same for this configuration. **(C)** To fix this problem, the two unbound electrons of the nitrogen atom form a lone pair, and two of the three electrons of the carbon atoms neighbouring the vacancy will form a quasi covalent bond. This configuration leaves one electron at the vacancy, and is known as the NV^0 center. **(D)** For a NV^- center, an additional electron from the lattice is needed to form a spin 1 system.

electrons can now form a spin 1 system, and have convenient properties for us, like optically detected magnetic resonance (ODMR), which is discussed in the next section. Even though this system technically is a negatively charged NV center, or NV^- center, it is, due to its popularity, often referred to simply as NV center, e.g. in this thesis.

2.2 Level scheme and Optically detected magnetic resonance

The NV center's lattice structure reflects itself in its energy spectrum illustrated in figure 2.2 - as we are dealing with a spin 1 system, we have both a singlet as well as a triplet state, though the singlet state is not strictly necessary in order to understand ODMR.

We also have a ground- and an excited state, seperated by a zero phonon line at 637 nm. In our experiments however, we will not observe this zero phonon line, as at nonzero temperatures this line is weakened, and the excitation spectrum is shifted to higher energies, while the fluorescence spectrum is shifted to lower frequencies, with the additional energy being converted into vibrational energy in the lattice. This is due to the Franck-Condon principle, briefly explained in appendix A.

The ground excited state has a zero field splitting $D \approx 2.87\,\text{GHz}$, as it is energetically favourable for two electrons to be in different spin states (as is the case for the $m_s = 0$ state) compared to the same spin state, where their spatial wavefunctions

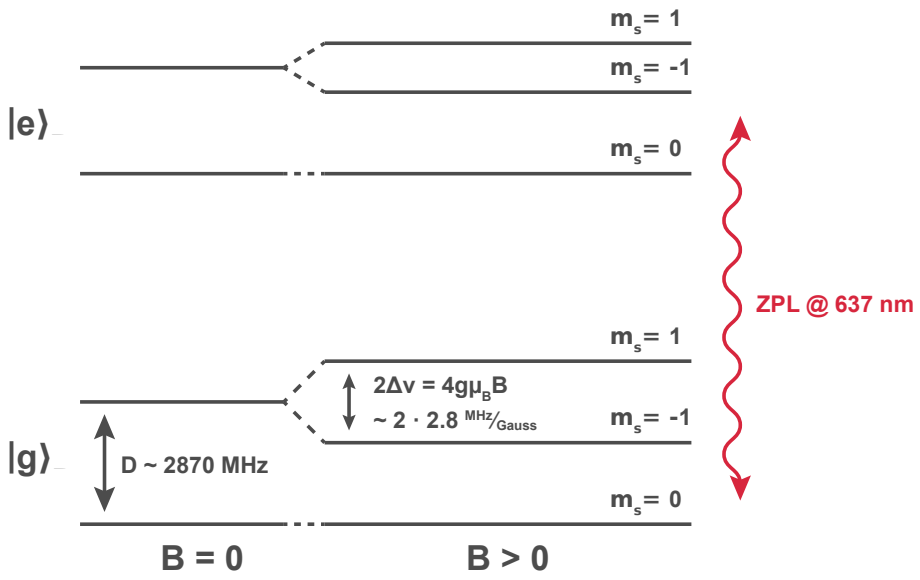

Figure 2.2: Simplified NV center level scheme.

need to be different due to the Pauli exclusion principle.

What we can now use to measure the magnetic field is the Zeeman shifts of the $m_s = \pm 1$ states. As we have a two electron system, the energy levels shift with

$$\Delta\nu = 2\gamma_e \cdot B \approx 2.8\text{MHz/Gauss} \tag{2.1}$$

Here γ_e is the gyromagnetic ratio of the electron.

One useful property of the NV^- center is, that the excited $m_s = \pm 1$ states are more likely than the $m_s = 0$ state to decay back to the $m_s = 0$ ground state nonradiatively, as shown in figure 2.4.

One can make use of this by chirping a microwave across the two transitions, and at the same time exciting the NV centers from the ground- to the excited state - if the microwave is tuned either to the $m_s = 0 \rightarrow m_s = -1$ or the $m_s = 0 \rightarrow m_s = 1$ transition, we see a dip in the fluorescence, as illustrated in figure 2.3. Conveniently, due to the Franck-Condon principle, we can use a green laser to excite the NV centers, and separate the fluorescence using a longpass filter at 650 nm.

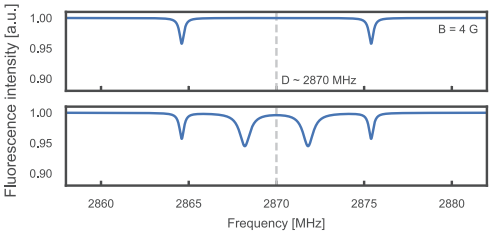

Figure 2.3: In our samples all possible NV center orientations exist. Here

To improve the signal to noise ratio of this signal, we perform these measurements not on a single defect, but on ensembles of many defects in a single diamond. How-

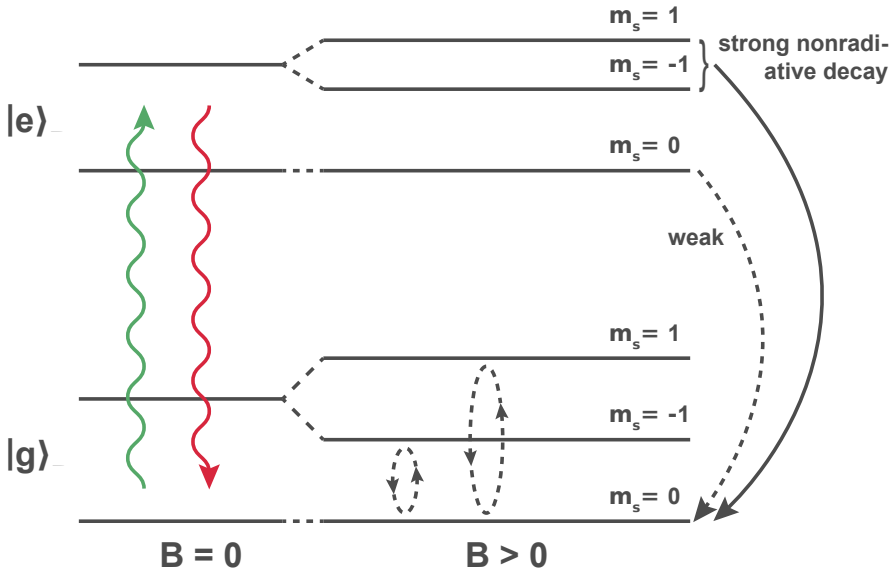

Figure 2.4: Reading out the magnetic field using optically detected magnetic resonance (ODMR)

ever, these NV centers will generally be aligned randomly in the diamond lattice, as four different orientations are possible (see figure 2.5). This leads to us not only seeing those dips at $\Delta\nu = \pm 2\gamma_e B$, but also at $\Delta\nu = \pm 2\gamma_e B \cdot \cos(109.5°)$ (as shown in figure 2.3), where $\cos(109.5°)$ is the tetraeder angle coming from the diamond's lattice structure.

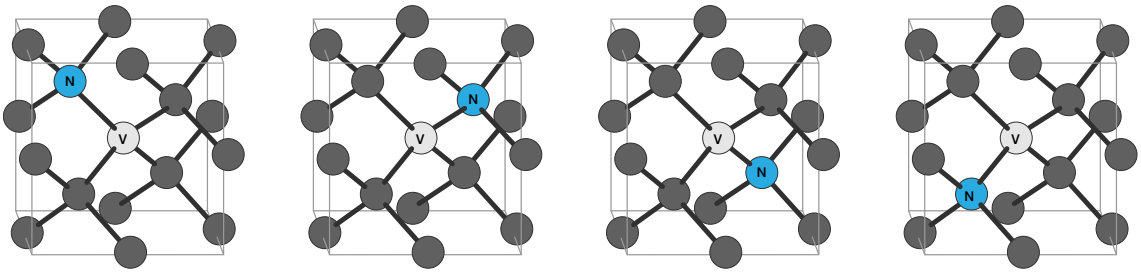

Figure 2.5: Due to the symmetry properties of diamond, NV centers can exist in four orientations in a single lattice. Electronic connections of the diamond lattice have been kept for geometric visualization.

2.3 Shot noise

One fundamental limitation of the precision achievable when measuring the magnetic field is the shot noise in the fluorescence collected on the photodetector used for readout. As in the photodiode every photon detected will free one electron, we get a current noise $\Delta I = \frac{e}{\Delta t} \cdot \sqrt{n}$, where e is the elementary charge, and n is the number

of photons detected over a time interval Δt.

The photocurrent in the photodiode can now be expressed as $I = \frac{e \cdot n}{\Delta t}$ using the same notation. Plugging this into the previous equation after solving for n now yields:

$$\Delta I = \sqrt{\frac{e \cdot I}{\Delta t}}$$

We can also conveniently express Δt in terms of frequencies, where one has to consider that both positive as well as negative frequencies contribute to the time interval Δt: $\Delta t = 2 \cdot \Delta f$, where Δf now is the single-sided bandwidth of the measurement. Plugging this in yields:

$$\Delta I = \sqrt{2 \cdot e \cdot I \cdot \Delta f} \tag{2.2}$$

This noise in photocurrent fundamentally limits the precision, with which we can determine the position of features in the NV center's ODMR spectrum, and therefore the magnetic field strength, in a given time.

3 Signal generation and readout

The following chapter will describe the setup used for measuring the magnetic fields shown in figure 3.1, split up into three parts:

Signal readout: A system for extracting the information about the magnetic field strength from the fluorescence is needed. This system also needs to have some access to a microwave source, because its frequency sets the magnetic field strengths that can be measured

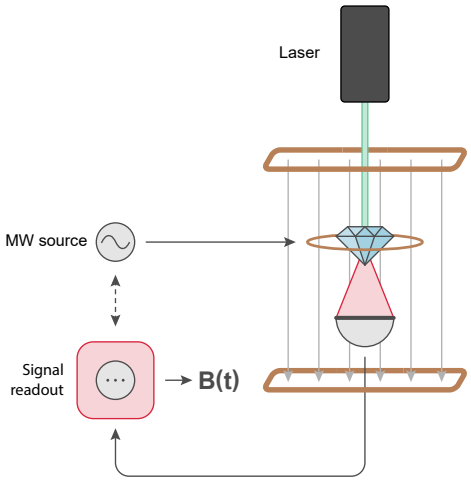

Figure 3.1: Simplified magnetometry setup.

Optical setup: In order to read out the spin state of the NV centers, we want to make use of optically detected magnetic resonance. This means, that we need a laser to excited the transition from $|g\rangle$ to $|e\rangle$, and some sort of optical setup to collect the fluorescence emitted by the sample.

Microwave source: In addition to that, a microwave source is needed to drive the transitions $m_s = 0 \rightarrow m_s = -1$ and / or $m_s = 0 \rightarrow m_s = 1$, such that their Zeeman shift can be employed.

3.1 Signal readout

The first thing one needs to consider when designing a NV center magnetometry setup is, how the fluorescence signal can be converted into a magnetic field reading. For our purpose, it is very important that the magnetic field signal is available in real time, because we are planning to use it as an error signal for a feedback loop. Latencies in the signal processing lead to phase shifts in the measured signal, limiting the bandwidth of the feedback loop.

One common way of determining the magnetic field applied to NV centers is to chirp the microwave across the spectrum, and to fit some curves to the dips in the fluorescence. This would clearly not work for us, because in order to reach even just

a 1 kHz control loop bandwidth, we'd need to chirp the microwave and perform a fit at least every 500 μs.

3.1.1 Lock in amplification

An approach allowing to read out the magnetic field in real time is to use lock in amplification: By frequency modulating the microwave tone we send in, we can generate an error signal which is proportional to the derivative of the ODMR spectrum (see figure 3.2). If we now tune our microwave to be near its zero crossing, the error signal is approximately proportional to the magnetic field fluctuations (minus a constant offset determined by the microwave frequency).

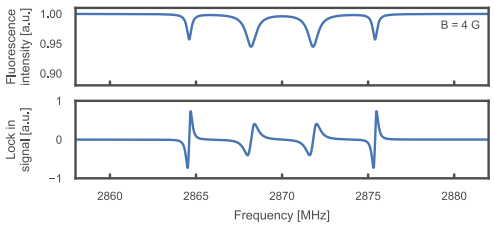

Figure 3.2: By using a lock in scheme the derivative of the ODMR spectrum can be measured.

This scheme works by frequency modulating the microwave frequency ν with the lock in frequency ω_{mod}, which is much larger than the fastest dynamics in the spectrum. Because of this, the detected Intensity $I(\omega)$ at a given frequency component is not constant any more:

$$I(\omega) \rightarrow I(\omega + A_0 \cdot \sin(\omega_{mod} t))$$

Typically, we want to use lock in amplifiers in the regime, where the frequency modulation depth A_0 is significantly smaller than the size of any features of interest in the spectrum. Then we can approximate the intensity with the first order Taylor expansion around frequency ω_0:

$$I(\omega + A_0 \cdot \sin \omega_{mod} t) \approx I(\omega_0) + A_0 \sin(\omega_{mod} t) \frac{dI}{d\omega}\Big|_{\omega=\omega_0} + \ldots$$

The zeroth order term of this expansion is approximately constant, because it evolves much slower than the lock in frequency, and will typically be filtered out by AC coupling the input of the lock in amplifier as it's not of much interest.

From the remaining terms we can now reconstruct the derivative $\frac{dS}{d\omega}$ of the actual ODMR spectrum by multiplying again with the modulation frequency:

$$I\left(\omega + A_0 \cdot \sin\left(\omega_{mod} t\right)\right) \cdot \sin\left(\omega_{mod} t\right) \approx$$
$$A_0 \sin\left(2\omega_{mod} t\right) \frac{dI}{d\omega}\Big|_{\omega=\omega_0} + \frac{A_0}{2} \frac{dI}{d\omega}\Big|_{\omega=\omega_0} \tag{3.1}$$

By applying a low pass filter to this signal we can filter out the term oscillating with $\sin\left(2\omega_{mod} t\right)$, leaving us with the lock in output $S(\omega)$:

$$S(\omega) \approx \frac{A_0}{2} \frac{dI}{d\omega}\Big|_{\omega=\omega_0} \tag{3.2}$$

However, this is only true, if the frequency modulation depth A_0 is much smaller than any feature of interest in the spectrum.

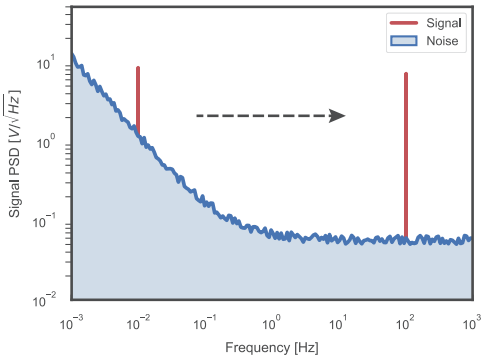

Figure 3.3: Lock in amplification allows to detect signals at higher frequencies in order to avoid noisy backgrounds.

One benefit of this setup is that the noise collected by the signal in the signal chain can be reduced: With this scheme the signal can be shifted to arbitrary frequencies, so that detection in frequency bands with a lot of noise in the signal path can be avoided (see figure 3.3).

Lock in schemes works best if the phase difference between the oscillation inputted into the lock in amplifier and the lock in's internal oscillator is zero. This is not necessarily the case, as typically fairly high lock in frequencies are chosen to avoid $1/f$ and similar noise sources, and to work in the band with the lowest noise available. That can induce a phase shift at the lock in frequency, so most lock in amplifiers allow to adjust the phase of the demodulation oscillator to compensate for this, and maximize the signal to noise ratio.

The phase setting can also be employed to measure the signal path's noise floor: By shifting the lock in's phase by 90°, no signal is present in the lock in output anymore, and any remaining output is background noise.

3.1.2 Data processing on a FPGA

In a feedback loop one generally wants the error signal to have as little noise as possible, or at least as little noise as necessary. Unfortunately, many analog circuits

introduce noise at some point, making the lock in amplifier's output noisier again. To prevent this, and keep the setup as compact as possible, the whole error signal generation as well as the PID controller have been realized on a Field Programmable Gate Array (FPGA).

While microprocessors are a simple way of digitally processing data, they are not very fast at doing that - the latencies would make it impossible for us to generate an error signal with 1 kHz of bandwidth or larger. A FPGA however does not execute a software on a given hardware like a microprocessor does, but reconfigures its hardware to execute the task instructed to do, which allows to keep latencies low, often below 1 μs.

Unfortunately, programming FPGAs is quite a lot of work, especially if one wants to be able to reconfigure the task they are doing slightly without recompiling a new bitstream. PyRPL [34] is a modification of the original RedPitaya's FPGA code, allowing to reconnect different modules - for instance PIDs, IQ modulators, arbitrary waveform generators, or infinite impulse response filters - via Python. PyRPLs code was used as a basis for modifications - described in more detail in appendix B.2.

An overview over the functionalities implemented on the RedPitaya's FPGA is given in figure 3.4: The output of the photodiode is directly fed into a lock in module (the bright box), demodulating the signal. Its reference oscillator modulates the frequency of an arbitrary waveform generator. Sidebands at about 2.2 MHz distance are added before outputting the oscillations to be used in the microwave setup.

This exists twice on the FPGA to compensate for temperature fluctuations of the sample, as described in 4.2. In order to obtain a compensated magnetic field reading, the two lock in outputs are subtracted in the end.

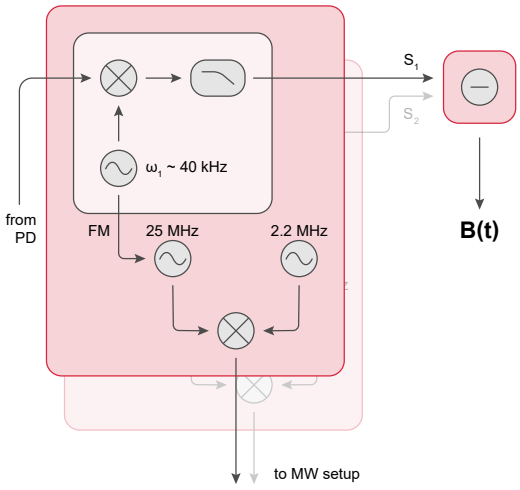

Figure 3.4: Overview over the tasks performed on the FPGA.

3.2 Optical setup

The optical readout of NV centers allows to extract information about the spin state of the NV centers, and thus to measure the magnetic field. For yielding good signal to noise ratios however, great care has to be taken into not introducing noise into the fluorescence signal.

The workhorse in this setup is the autobalanced photodetector (a Newport Nir-

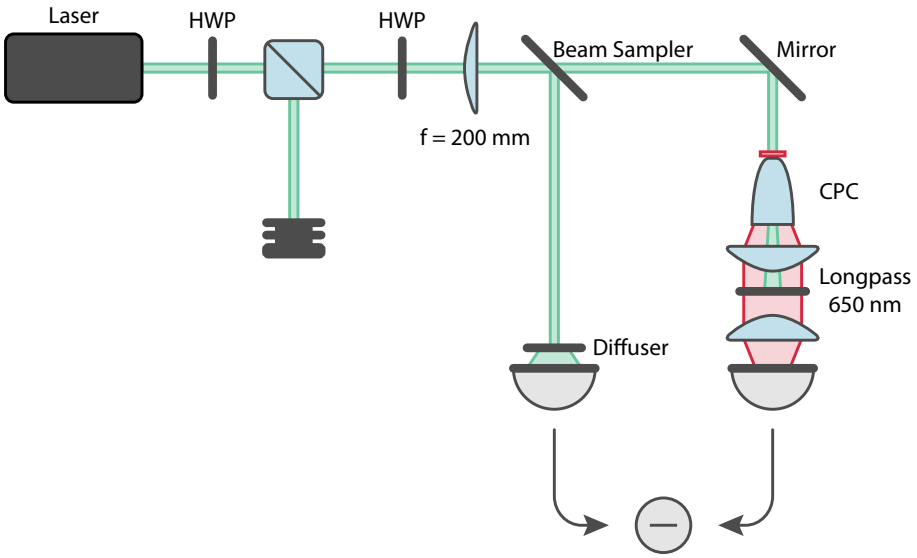

Figure 3.5: Optical setup used for collecting the sample's fluorescence.

vana 2007), allowing to cancel correlated noise between the NV center's fluorescence and a reference beam provided by the laser.

This means, that the main design considerations for the optical setup are to prevent the introduction of laser noise after splitting the reference beam from the excitation beam, and to collect as much fluorescence from the NV centers as possible to reduce intrinsically uncorrelated noise between the two arms (like photon shot noise).

This also means, that the laser intensity noise present before splitting the reference beam from the excitation beam does not matter too much, as long as the polarization of the beam is well defined (a fluctuating polarization might lead to intensity differences between the reference and excitation beams). Using a 1 W 520 nm laser acquired off Ebay noise levels corresponding to four times the shot noise limit could be reached for about 2.5 mW of collected fluorescence.

In figure 3.5 the setup used for illuminating the sample and collecting the fluorescence is shown. The laser beam is initially sent through a half wave plate and a polarizing beam cube, allowing to adjust the intensity of the excitation beam, and cleaning up its polarization to prevent polarization noise turning into intensity noise later on. Another half wave plate is used to set the reflectivity of a beam sampler, and provides the reference light. Before the photodiode, a diffuser is used to remove etalon noise in the beam, which would be uncorrelated between the two signals, and could not be cancelled by the autobalanced photodetection.

3.2.1 Autobalanced Photodetection

Extracting a small optical signal from a large offset is generally hard, as the signal has to be distinguished from fluctuations of the offset. The main idea behind balanced photodetection is that fluctuations in the source laser power will translate linearly into fluctuations of the signal. This allows one to just measure both, and subtract them to recover the initial signal. A simple circuit that outputs the difference between two photocurrents is shown in figure 3.6.

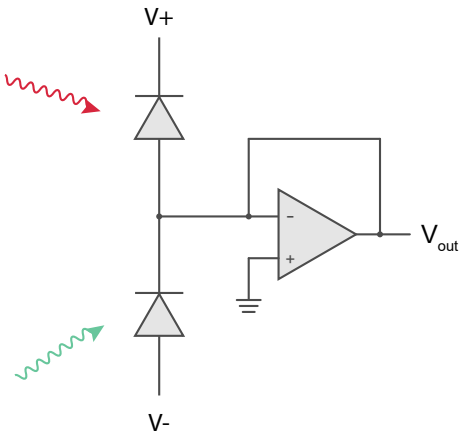

Figure 3.6: Functioning of a balanced photodetector.

However, for subtracting the two signals, one needs to normalize them against each other - the two measured photcurrents need to stay constant. Typically, their relative intensities will not stay constant - for instance thermal effects, or acoustial vibrations can slightly misalign the beams. A circuit that compensates for that is the autobalanced photodetector [35, 36]: A low-passed version of the difference in the two photocurrents is used to compensate for differences in intensity on the photodiodes.

In 3.7 the schematic of an autobalanced photodetector is shown: Similarly to the balanced photodetector, the two photodiodes D1 and D2 detect the signal and the reference beam. The difference lies in the use of the transistor pair Q1 and Q2: The

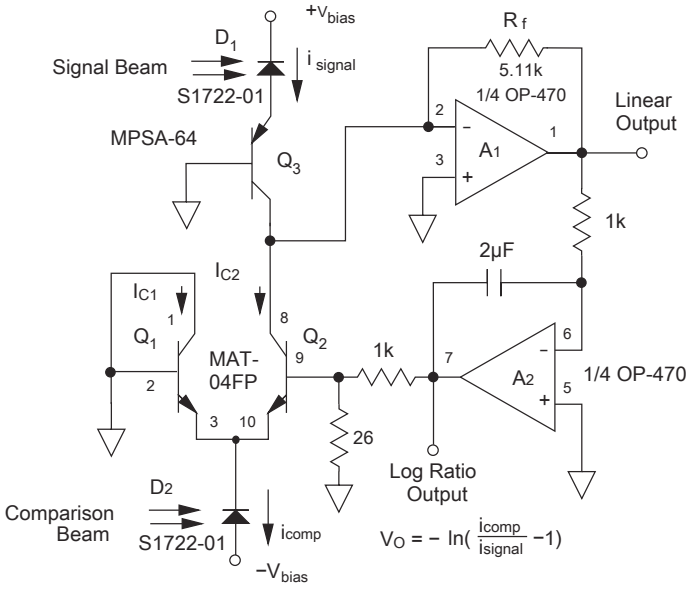

Figure 3.7: Schematic of an autobalanced photodetector. Taken from [36]

photocurrent of D1 will travel through Q2 and D2 afterwards, no matter what, but if the photocurrent of D2 is larger than the one through D1, additional current can flow through Q1. This means, that by changing the base current at Q2, we can set how much current will flow through Q1 and Q2. With that, we can regulate the voltage at the collector of Q2 to be zero, so the two photocurrents cancel here. Now we can amplify this voltage with A1 to recover our signal.

The voltage at the base of Q2 is regulated by A2, forming a feedback loop to stabilize the voltage at the collector of Q2 to ground. The bandwidth of this feedback loop must be significantly smaller than any frequencies of interest, to ensure that the signal is not regulated away. However, the feedback loop's bandwidth does not need to be large, as the noise cancellation does not come from the feedback loop, but from the two photocurrents being subtracted, and can work up to much higher frequencies.

All in all, this circuit allows to reduce the influence of laser noise down to shot noise level for AC measurements.

3.2.2 Compound Parabolic Concentrators

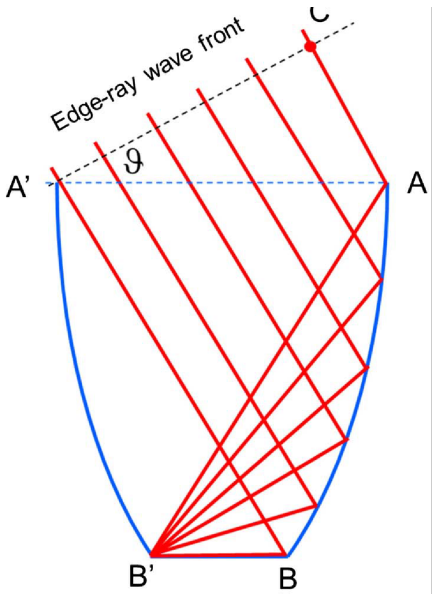

Figure 3.8: Construction of a compound parabolic concentrator from a rotated parabola - B' is the focus of parabola A. Figure taken from [37].

In the previous section it was discussed, how correlated noise in the sample's fluorescence can be reduced down to the shot noise limit. Once this is achieved however, shot noise has to be reduced. For this it is important to collect as many fluorescence photons from the NV centers as possible.

Here, the conservation of etendue is limiting the collection efficiency, because the etendue G is conserved:

$$dG = n^2 dS \cos\theta d\Omega \tag{3.3}$$

Here n is the refractive index of the medium, dS is a differential surface element the light is propagating through, θ is the angle between the surface's normal and the light propagation direction direction and $d\Omega$ is the differential solid angle the light is propagating under.

By looking at equation 3.3 the complication in collecting much fluorescence becomes clear: The fluorescence of our sample is emitted over the whole surface area

of the diamond, and ideally we'd like to collect all fluorescence emitted under a 2π solid angle. The only way this angle can be reduced is by increasing the area dS at the same time.

If the main requirement is to collect as much fluorescence as possible, non-imaging optics [38, 39] outperforms imaging optics significantly. One component acting right on the limits set by equation 3.3 is the compound parabolic concentrator, illustrated in figure 3.8: All light emitted under 2π on the lower surface will be collected and emitted on a larger surface, but under smaller angles. Light coming in on the upper surface under larger angles will be reflected out again, and, due to the reversibility of the light path, there is no scenario where light from the lower surface will be reflected out under such an angle.

To prevent the light beam from widening further, the optical paths have to be kept as short as possible, so that the photodiode is located about 5 cm away from the sample, even with two short focal length aspheric lenses in between.

3.3 Microwave setup

Special attention has to be given to the microwave signal generation, as this is the component, which will perform spectroscopy on the Zeeman levels, so that microwave noise will lead to noise in the error signal. The main concern here are spurs - microwave signals generated at new frequencies by higher order processes, e.g. in a saturated amplifier.

It would be best practice to keep the different microwave signals at frequency ν_1 and ν_2 separated for as long as possible, and to combine them only after amplification, but as size and complexity of the setup are important design considerations, they are already combined before the high power amplifier. A sketch of the microwave setup is shown in figure 3.9.

The two microwave tones are generated independently at first: The frequency modulated output of the RedPitayas (already containing sidebands at $\approx 2.2\,\mathrm{MHz}$) is first high pass filtered (using a MiniCircuits ZFHP-0R50-S+ high pass filter). This filter will allow us later on to use a low passed version of the DAC signal as a control signal for regulating the current through a Helmholtz coil pair. This high pass filter is used in both paths for symmetry reasons.

Afterwards, the high pass filtered signal is mixed (using MiniCircuits ZX05-43H-S+) with a microwave signal generated by one channel of a Windfreaktech SynthHD. A mixer is a component which multiplies two input voltages:

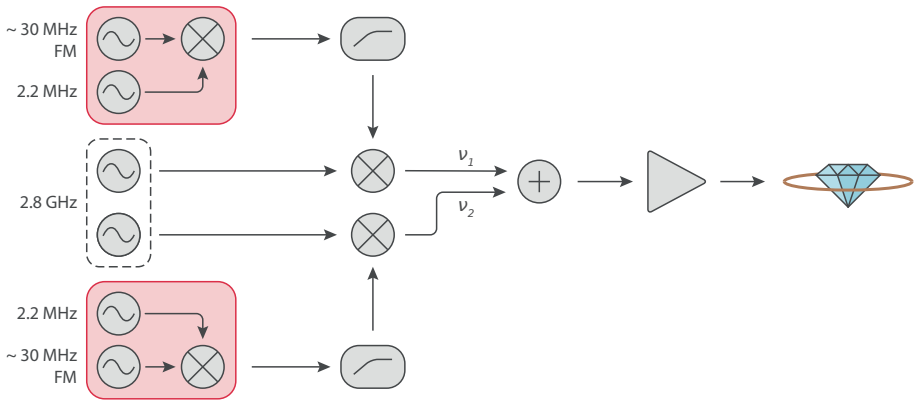

Figure 3.9: Microwave setup for dirving the $m_s = 0 \rightarrow m_s = -1$ and the $m_s = 0 \rightarrow m_s = -1$ transitions. The two red boxes are the two DACs of the RedPitaya, and the oscillators in the dashed box are the two output channels of one SynthHD.

$$A_1 \sin(\omega_{LO} t) \cdot A_2 \sin(\omega_{IF} t) = \frac{A_1 A_2}{2} \cdot [\cos((\omega_{LO} - \omega_{IF})t) - \cos((\omega_{LO} + \omega_{IF})t)] \quad (3.4)$$

Here LO stands for local oscillator - for us, that is the output of the SynthHD at about 2.8 GHz, and IF stands for intermediate frequency - the output of the RedPitaya, which is typically in the range of 30 MHz. That means, that by using the mixer, we created two microwave tones at frequencies $\omega_{LO} - \omega_{IF}$ and $\omega_{LO} + \omega_{IF}$. Care has to be taken to not saturate the mixer, as otherwise additional frequencies can be created.

As both microwave tones are frequency modulated with the same lock in frequency, they can both lead to measurable signals in the lock in amplifier. To avoid measuring signals at both frequencies, the local oscillator frequency is chosen such that the unused sideband faces away from the zero field splitting, where no features are expected. In case the second sideband becomes problematic, a single sideband mixer - for instance created with a 90° hybrid and an IQ mixer - can supress this sideband, so that only one frequency modulated microwave tone is generated.

After that, the outputs of the two mixers are added together using a power splitter (MiniCircuits ZX10-2-442-S+) and fed into a high power amplifier (MiniCircuits ZHL-16W-43-S+). Care has been taken that this amplifier does not saturate, because this would create spurs at additional frequencies. For the same reason, no preamplifiers were used. The microwave power applied to a wire loop around the sample was chosen such that power broadening of the microwave transitions does not limit the precision of the error signal generated.

All in all, a compact, and comparatively cheap setup for performing magnetometry on NV centers has been demonstrated in this chapter. Using noise reduction techniques like lock in amplification and autobalanced photodetection made the use of comparatively cheap components, like a 1 W, 520 nm laser bought off Ebay, possible.

The microwave setup needed for performing spectroscopy on the NV center's Zeeman shift can be kept relatively compact by performing the frequency modulation needed for the lock in scheme and the mixing with the hyperfine splitting already on the RedPitaya's FPGA.

Additionally, compound parabolic concentrators have been discussed briefly - as collecting as much fluorescence as possible from the NV centers is important for a good noise performance, they play a key role in keeping the measurement noise low.

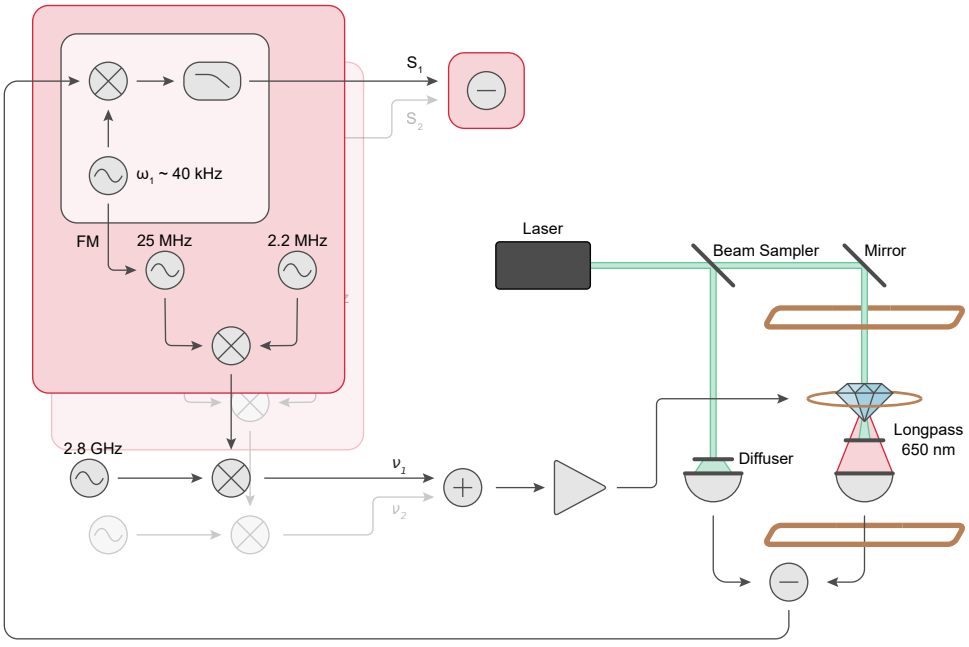

Figure 3.10: Overview over the whole experimental setup used.

4 NV center magnetometry

While the setup described in the previous chapter is the setup I used for the stability measurements in chapter 5, quite some experimenting was needed to converge to this setup. The following chapter will describe some of the measurements done to identify noise sources present in the setup, and show ways of reducing the influence of these sources.

4.1 Identification of noise sources

When performing magnetometry with the setup described in the previous chapter, one might measure a spectrum similar to the one shown in figure 4.1: One can clearly see a broad peak at low frequencies, introducing magnetic field noise up to several hundreds of μG at frequencies up to 300 Hz. This noise is introduced by our power supply driving the magnetic field coils. The band in which this noise is introduced is not necessarily as narrow as it is in our measurements, but it depends on the electromagnet's inductance and the power supply's output capacitance: Both form an underdamped second order low pass filter, preventing current from going through the magnetic field coils after the resonance frequency.

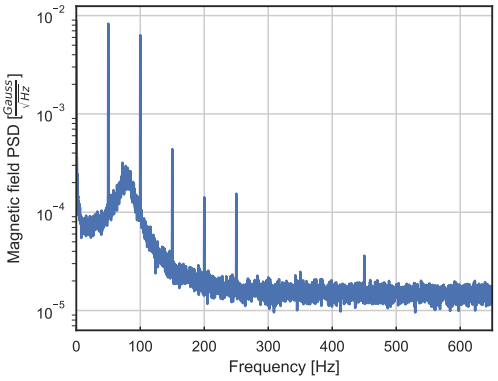

Figure 4.1: Spectrum of the magnetic field reading of the NV centers. There appears to be a white noise floor at about 18 $\mu\mathrm{G}/\sqrt{\mathrm{Hz}}$.

Another magnetic field source one can clearly see in this measurement is the noise introduced at 50 Hz and harmonics by the power line, creating about 10 mG of magnetic field noise in our setup.

However, there is also a white noise floor visible in this spectrum. One might assume, that this noise is Johnson noise in a shunt resistor used in the power supply driving the magnetic field coils, but shifting the phase of the lock in amplifier by 90°clearly shows that this noise is not magnetic field noise.

What one can do now to investigate the noise is to change parameters in the experiment, and observe how the noise behaves. A measurement of the noise floor

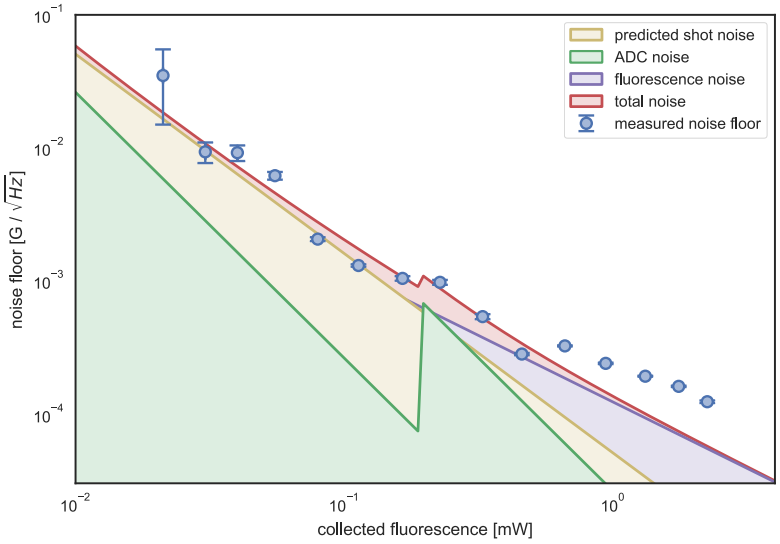

Figure 4.2: Position of the measurement noise floor vs. collected fluorescence. Each data point corresponds to a single measurement of the noise floor, so no statistical fluctuations between different measurements were considered. The strong fluctuations in noise floor stem from the autobalanced photodetector, as the splitting ratio of the signal- and reference beam had to be set manually.

for varying excitation laser power (and thus for varying collected fluorescence) is shown in figure 4.2. Different possible sources of noise have been drawn in, and will be discussed now:

ADC noise: The first possible noise source one might think about when looking for sources of noise is the quantization noise of the ADC used on the RedPitaya. This noise will stay constant independent of signal strength, so the signal to noise ratio will grow linearly with signal strength. A kink at about 200 μW collected fluorescence appears, because the photodiode gain had to be reduced by a factor 10 to not saturate the ADC.

Due to the high sampling rate of the RedPitaya, we can measure much more precisely than the naively expected quantization noise floor of $\frac{2\,\mathrm{V}}{2^{14}\cdot\sqrt{Hz}}$ for 14 bits, as the sampling rate of 125 MHz allows to integrate away noise outside our measurement bandwidth. For the most precise measurements so far, the RedPitaya's ADC noise floor was still about 20 dB lower than other noise sources. If this noise floor would be dominating at some point, a more precise ADC would be needed.

Photon shot noise: From equation 2.2 we know the level of shot noise present in the photocurrent we measure in the photodetector. This can be used to calculate the shot noise in the magnetic field reading, using the inverted lock in ramp $\frac{df}{dS}$, the

gain of the photodetector and the lock in amplifier R (keeping in mind the factor 2 dropped by the lock in detection), as well as the gyromagnetic ratio of the electron γ_e:

$$\Delta B = \frac{df}{dS} \cdot \frac{R}{2\gamma_e} \cdot \sqrt{2 \cdot e \cdot I \cdot \Delta f} \tag{4.1}$$

From this equation we see how the signal to noise ratio can be improved further, if we are dominated by shot noise: Clearly, we can increase the amount of fluorescence collected by the autobalanced photodetector, which will decrease the shot noise in the signal by a factor of $\sqrt{I}$. However, after about 3 mW of light incident on the signal photodiode, the internal electronics of the autobalanced photodetector start to saturate, leading to the output signal either drifting to the supply rails or to the noise suppression quality decreasing again.

The other option is to increase the signal contrast, e.g. by using higher microwave power, or by adding sidebands at roughly 2.2 MHz separation to address all three hyperfine features (these can be seen in an actually recorded ODMR spectrum, as in figure 4.3). At some point however, higher microwave powers lead to a broadening of the NV center's resonance, decreasing the lock in slope again. Additionally, if the amplifier is not operated in it's linear regime any more, additional frequencies will be generated, which can manifest themselves as noise peaks in the error signal.

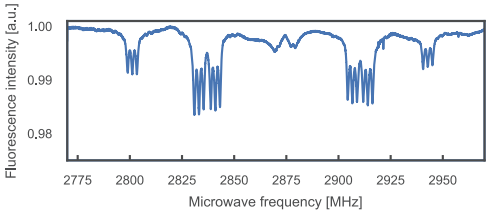

Figure 4.3: Recorded ODMR spectrum of the NV centers - one can clearly see the hyperfine splitting of each transition due to the interaction of the NV centers with neighbouring ^{14}N spins.

Ultimately, to improve signal to noise further if limited by shot noise, either a custom autobalanced photodetector would need to be built (which could be based on the description given in [36]), or a diamond with narrower linewidths could be used.

Fluorescence noise: Fluorescence noise occurs when the optical transition between the ground- and excited states in the NV centers saturates. This leads to laser noise not being mapped onto the fluorescence linearly, making the fluorescence signal less noisy than the laser. Because the functioning of the autobalanced photodiode relies on exactly this assumption, the laser noise in the reference beam cannot be substracted from the fluorescence signal as efficiently any more.

The fluorescence noise visible in figure 4.2 was caused by the waist of the excitation laser beam being too small at the sample, saturating the NV center transitions

locally. By shifting the laser's focus this noise could be removed again. If the whole sample was saturated, one would either have to modify the functioning of the autobalanced photodetector, or simply use a sample containing more NV centers.

4.2 Temperature noise suppression

Unfortunately, there are not only external sources of noise when measuring magnetic fields with NV centers, but also intrinsical ones: The zero field splitting D is not at a constant position, but depends on the lattice constant of the diamond, which depends for instance on temperature [40]. As a growing lattice constant leads to a decreased probability of the two electrons in the NV^- center to have the same spatial wavefunction, the energy penalty for both of them being in the same spin state decreases, too.

This shift is about $-74\,\mathrm{kHz/K}$ at room temperature, which means that an active temperature stabilization of the diamond would not be feasible - even with a temperature stability of 100 mK we would get fluctuations in our magnetic field reading on the order of 3.7 mG when only monitoring one of the transitions, much larger than any of the contributions discussed in the previous section for measurement bandwidths of 1 kHz.

A fairly effective solution is to adhere the sample to a heatsink, and let it thermalize, as shown in figure 4.4. While the temperature of the diamond just connected to the compound parabolic concentrator fluctuates by about 3 °C, the heatsunk sample's temperature fluctuations cannot be detected by the independent magnetic field sensor any more.

However, this does not fully eliminate temperature fluctuations so that we will need to actually determine the position of both transitions $m_s = 0 \rightarrow m_s = -1$ and $m_s = 0 \rightarrow m_s = 1$ in order to distinguish between a moving zero field splitting D or magnetic field fluctuations.

In figure 4.5 a scheme for extracting the magnetic field reading by monitoring both transition frequencies ν_1 and ν_2 is shown: Modulating the two microwave tones with different lock in frequencies allows to extract an error signal for both transitions. While these error signals are out of phase for magnetic field fluctuations, they are in phase for temperature fluctuations, so adding / subtracting the two signals yields a pure magnetic field / temperature signal, with up to 46 dB suppression of the other component. The magnetic field signal can now be used to regulate the magnetic fields in our experiment, while the temperature signal can be used to slowly adjust both microwave tones ν_1 and ν_2, to prevent the transitions from drifting away underneath the tones.

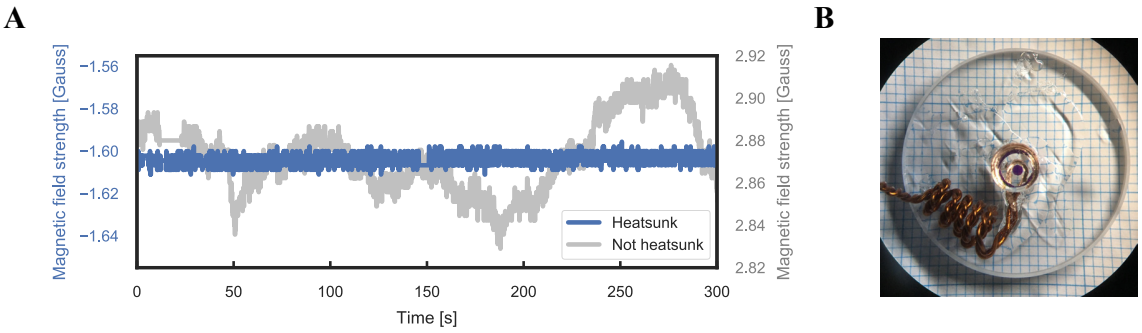

Figure 4.4: **(A)** Comparison of a magnetic field stabilized to the transition $m_s = 0 \rightarrow m_s = +1$ of a not heatsunk sample (in grey) to the same sample adhered to a piece of sapphire glass (in blue). Both fields have been measured by a LSM303DLHC, read out by an Arduino Uno. One clearly sees slow drifts of the measured magnetic field in the first measurement, that disappear if the sample is heatsunk. **(B)** Mounting of the diamond to the sapphire glass, viewed from the top (on 1 mm square graph paper): The diamond (the violet circular disk, about 1 mm in diameter) was glued to the sapphire glass plate (the transparent, 25 mm diameter disk) using M-GLAS by Merck. The compound parabolic concentrator is adhered to the other side of the diamond, and a wire loop acting as a microwave antenna is glued in place around the diamond, with some additional turns acting as a strain relief. The assembly was mounted into a SM1 lens tube afterwards, with an SMA connector soldered to the antenna, and a glass plate glued to the open side of the assembly to support the compound parabolic concentrator.

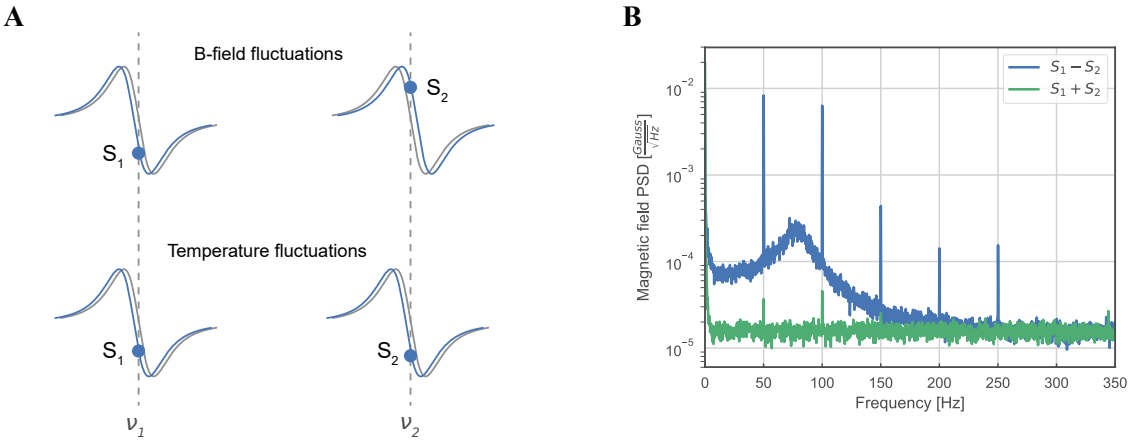

Figure 4.5: **(A)** While for magnetic field fluctuations the two transitions $m_s = 0 \rightarrow m_s = -1$ and $m_s = 0 \rightarrow m_s = 1$ move apart / together, for temperature fluctuations they move in one direction. If we extract error signals at both transition frequencies ν_1 and ν_2, they will be out of phase for magnetic field fluctuations, and in phase for temperature fluctuations. **(B)** If we add and subtract the normalized error signals, we can recover a pure magnetic field error signal. Magnetic field noise in the temperature signal is suppressed by up to a factor 200 and vice versa.

In order to quantify the quality of our error signal, it is also interesting to determine the amount of photon shot noise contributing to its white noise floor. Here, a photocurrent of 1.7 mA is generated in the signal photodiode [1], and we have a lock in slope of 1.38 $\frac{\mathrm{V}}{\mathrm{MHz}}$, as well as a total gain of 1 600 000 $^{\mathrm{V}}/_{\mathrm{A}}$. Plugging this into equation 4.1, we yield $\Delta B_{shot} = 10\,\frac{\mu\mathrm{G}}{\sqrt{\mathrm{Hz}}}$. With the measured noise floor in the temperature drift compensated error signal of $\Delta B = 18\,\frac{\mu\mathrm{G}}{\sqrt{\mathrm{Hz}}}$ we are therefore less than a factor 2 away from shot noise, with the second dominating noise source most likely being laser noise not cancelled perfectly by the (saturated) electronics in the autobalanced photodetector.

[1] This number had to be extrapolated from photocurrent measurements at lower excitation laser powers, and a laser power measurement at the power used, because the signal output of the photodiode was already saturated.

5 Magnetic field stabilization

In the previous chapter I showed how to generate a magnetic field reading from the NV center's fluorescence, and how to reduce the noise sources present in this signal. To stabilize a magnetic field with this signal we now feed back this value to a pair of Helmholtz coils using a PID controller on the RedPitaya's FPGA. This pair of coils is different from the coils used to generate the offset field, as the current through a low inductance load is easier to control, and to stay within the current limits of our homebuilt current driver, described in appendix B.1.

If one now closes the feedback loop and looks at the behavior of the error signal, it quickly looks like the magnetic field noise has been reduced significantly. Unfortunately, this in loop error signal is now not trustworthy any more: Noise present in the error signal can be regulated away, too, but will be present in the magnetic field afterwards - so the influence of noise in the error signal on the magnetic field cannot be seen this way.

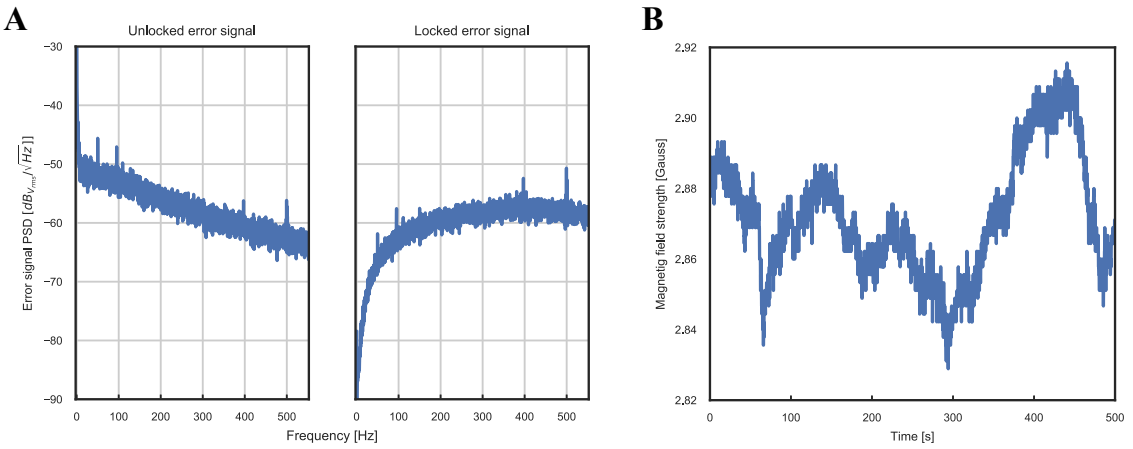

Figure 5.1: **(A)** Error signal spectrum for the magnetic field unlocked and locked to the error signal. **(B)** Even though the noise in the error signal decrased by about a factor 2, an independent magnetic field sensor measures much stronger fluctuations, because temperature fluctuations in the NV center error signal are also regulated away by the feedback loop. This shows the need for a second sensor confirming the functionality of the lock.

The only way to reliably test the realized stability is via an independent second sensor. For convenience, we decided to use a second diamond sample containing NV centers, but in order to keep the noise in both sensor signals uncorrelated, used independent optical and microwave setups

This also requires the two sensors to see the same magnetic field, even though they are at a distance. To ensure this, a large pair of Helmholtz coils was wound, and the magnetic field generated was simulated in advance using Radia [41]. According to the simulation, the magnetic field two samples at a 3 cm (as close as one can get the two samples located in their own SM1 lens tubes) distance experience should differ by less than 10 ppm - so as long as there are no strong magnetic field gradients present in the lab, the magnetic field (and its noise) seen by both sensors should be almost identical.

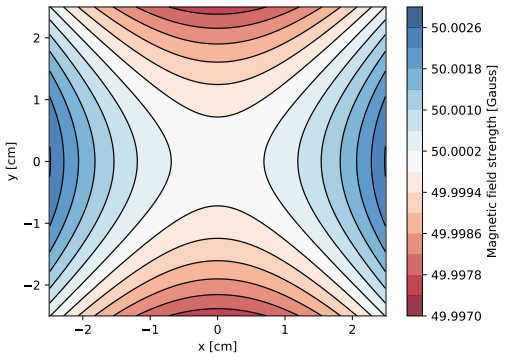

Figure 5.2: Simulated magnetic field of the Helmholtz coil pair used for the following measurements.

Now one of the two sensors can be used inside the feedback loop to stabilize the magnetic field, while the second sensor performs independent magnetic field measurements, ensuring that there is no systematic noise (e.g. temperature fluctuations, or spurs in the microwave spectrum) in the first sensor's reading.

As the AC noise in these measurements is still comparatively high, it is important to choose the control bandwidth appropriately - it is not possible to regulate the magnetic field signal below the sensor noise floor, so for too large control bandwidths additional noise will be introduced at frequencies, where no noise was present in the first place. As a compromise, a 1 kHz bandwidth was chosen, because no magnetic field noise above the sensor's noise floor is visible past this point.

5.1 Closing the feedback loop

In order to regulate the magnetic field, a PI controller on the RedPitaya's FPGA generates a control signal, that is then sent into our homebuilt current driver to regulate the current through the low inductance coil pair.

After just using a PI controller, some remaining noise peaks at 50 Hz and harmonics was present in the magnetic field. Commonly, a feedforward - an oscillating signal replicating the magnetic field noise triggered to the power line - would be used to remove this remaining noise. The problem about this approach is, that it relies heavily on the noise composition staying constant. This is typically not the case, and if the composition of noise frequencies changes the feedforward could even introduce magnetic field noise into the system.

The use of an FPGA for our control loop makes another scheme possible: Digital filters allow to taylor custom transfer functions, which can be used e.g. for removing

resonances from a system's transfer function to increase the control bandwidth [42], or in our case, to suppress noise at certain frequencies.

Conveniently, PyRPL [34] already has the functionality for creating and applying IIR filters built in. Summing it and our PI signal - instead of using the filter to build a transfer function for regulating the magnetic field by itself - made it possible to increase the P gain for very well defined frequencies only, as can be seen in figure 5.3 (C).

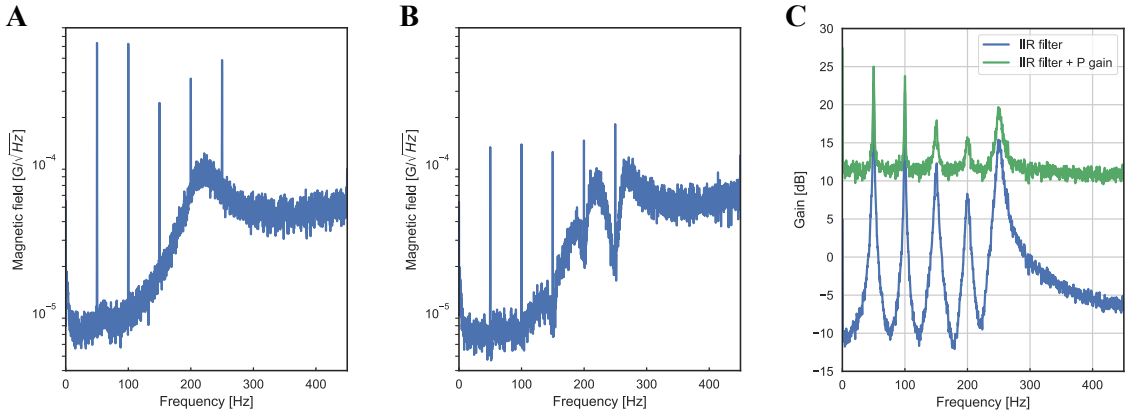

Figure 5.3: In-loop error signal before **(A)** and after **(B)** applying an IIR filter to suppress noise at 50 Hz and harmonics. **(C)** Gain of the IIR filter alone and combined with the P-gain of the PI controller.

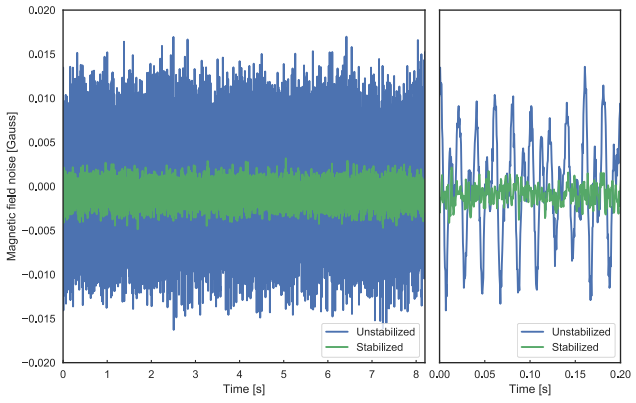

Figure 5.4: On the left: Locked and unlocked magnetic field, as measured on the independent second sensor. Right: The same data zoomed in into the first 0.2 s - the dominating noise source clearly is 50 Hz noise and harmonics.

Using the combination of PI controller and IIR filter, the magnetic field can be stabilized from 6.2 mG to 1.1 mG RMS noise over the control loop bandwidth. Considering our sensor noise floor of 18(1) $\frac{\mu G}{\sqrt{Hz}}$, the minimum noise achievable can be calculated as $18\,\frac{\mu G}{\sqrt{Hz}} \cdot \sqrt{1000\,Hz} \cdot \sqrt{2} = 805\,\mu G$, where the factor $\sqrt{2}$ stems from the noise contribution of both NV center samples (which have the same noise floor), that has to be considered.

This means, we are 35 % above the minimum achievable noise, so further improvements are unlikely without improving the sensor noise floor first. However, the sensor noise floor is a factor 2 above photon shot noise in the fluorescence, so in order to improve magnetic field stability the shot noise would need to be reduced.

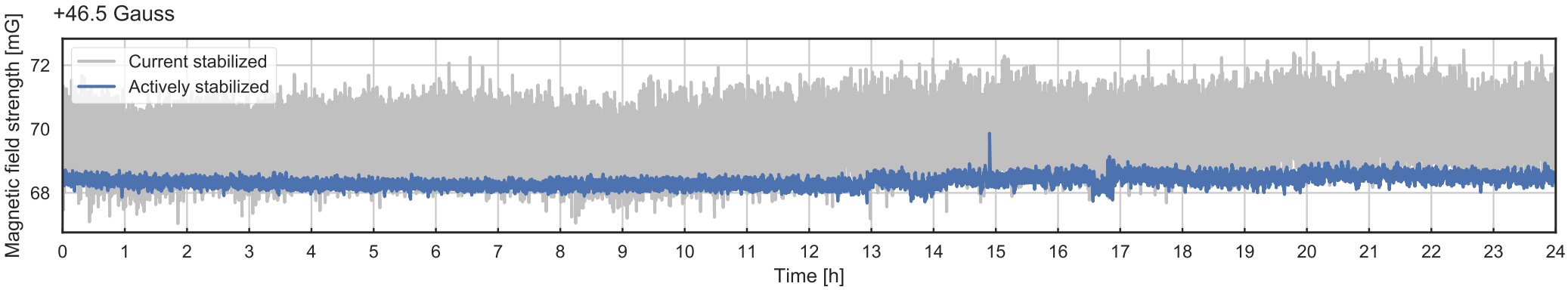

Figure 5.5: Longterm stability of the magnetic field measured over 24 hours with a 1 Hz bandwidth. While, if just the current through the Helmholtz coil pair is regulated, we have 610 μG RMS noise, this number decreases to 157 μG if the magnetic field is stabilized to the NV centers.

5.2 Long term stability

To test the long term stability of the magnetic field control, measurements of the locked and unlocked field were performed. To process the data, the sample rate had to be reduced, so the measurement bandwidth was reduced to 1 Hz on the FPGA, and slightly less than four magnetic field measurements were performed each second to sample the data appropriately. In addition to that, the microwave source was re-tuned once a minute to compensate for temperature drifts of the sample. These could potentially lead to the two resonances monitored drifting away. For this, $S_1 + S_2$ from the temperature noise compensation scheme could be used.

With this setup, measurements over 24 hours were performed for each case, the results are plotted in figure 5.5. Over the whole 24 hours the RMS noise in the stabilized magnetic field was 157 μG, in the not stabilized field it was 610 μG.

The current stabilized data trace was recorded during the weekend, at a time, where none of the experiments in the neighbouring labs were running. It is therefore expected for this noise to increase significantly during regular operation. The locked trace was recorded on a weekday, so the effect of other experiments running nearby can be seen from hour 13 of the measurement on.

5.3 Allan deviation

A standard measure for stability, most commonly used for characterizing oscillators and clocks, is the Allan deviation $\sigma_y(\tau)$ [43]:

$$\sigma_y^2(\tau) = \frac{1}{2(M-1)} \sum_{i=1}^{M-1} [S_{i+1} - S_i]^2 \tag{5.1}$$

Here τ is the time between two samples S_{i+1} and S_i, with S being a fractional B-field measurement $\frac{B(t)-B_{avg}}{B_avg}$. The time τ is varied to obtain the Allan deviation for different averaging times.

However, it is often more efficient to use the overlapping Allan deviation, as illustrated in figure 5.6. While the non-overlapping Allan deviation divides a measurement of N samples into M consecutive pairs separated by time τ, the overlapping

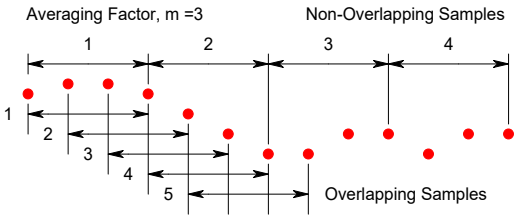

Figure 5.6: Difference in sampling of the overlapping and the non-overlapping Allan deviation. Figure taken from [43]

Allan deviation does not just use consecutive pairs, but all possible realizations. It can be calculated as:

$$\sigma_y^2(\tau) = \frac{1}{2m^2(M-2m+1)} \sum_{j=1}^{M-2m+1} \left\{ \sum_{i=j}^{j+m-1} [S_{i+m} - S_i] \right\}^2 \tag{5.2}$$

Here σ_y is the overlapping Allan deviation - so the square root of σ_y^2 in the equation. m is the spacing between two samples time τ apart - so m times as many realizations for pairs are considered for the overlapping Allan deviation. As this method forms the maximum number of pairs with averaging time τ, less data is needed to reach a set confidence level, making this the most commonly used measure of frequency stability.

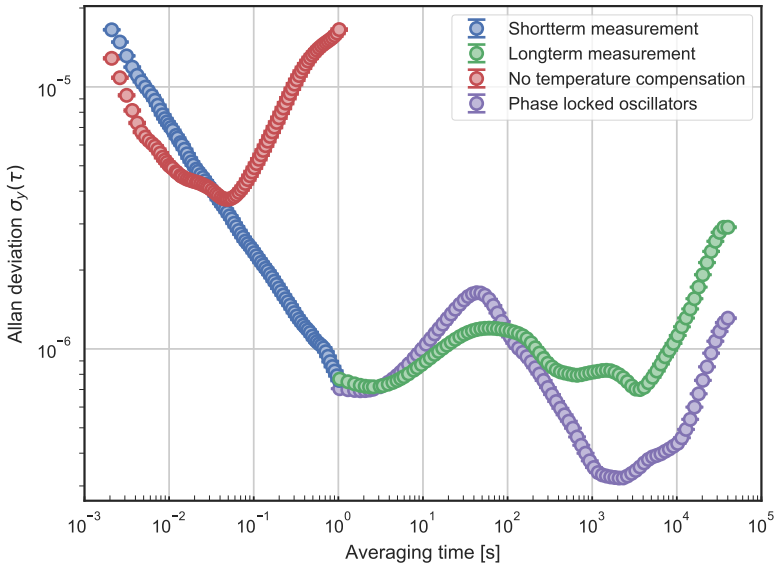

Figure 5.7: Allan deviation of the magnetic field noise at 40 Gauss. For the short term measurements the Allan deviation of five 8 s measurements was averaged to reduce the errors. The time trace of the long term measurement is shown in figure 5.5.

From the measurement of the magnetic field locked to a not temperature compensated sample, it is clear that the temperature noise compensation scheme is necessary: Without it temperature drifts dominate after less than a 100 ms averaging time. However, it leads to a decrease in precision, because we drive two transitions in the same defects simultaneously, decreasing signal contrast by a factor 2 for each of the two signals. Subtracting the signals from each other reduces that increase in noise by a factor $\sqrt{2}$, leaving us with $\sqrt{2}$ times more noise for the temperature drift compensated signal.

In the long term measurement, a striking feature is a broad peak at about 50 s

to 60 s integration time. This indicates that there is correlated noise present at this timescale - for us this is probably the re-tuning of the microwave sources once a minute, leading to a 5 s dead time. As this dead time was chosen pretty conservatively, and the times at which the re-tuning happens can be chosen freely, this is not expected to be problematic for our application.

Next, the Allan deviation decreases down to integration times of about 1 hour - afterwards, the Allan deviation increases again. This might be either the result of not fully suppressed temperature noise, or of frequency drifts in our microwave setup. The most likely source for frequency drifts is the reference of the SynthHD, as it is by far the highest frequency source - drifts of e.g. the RedPitaya reference would need to be roughly 100 times larger to have the same effect.

To test for this, both SynthHDs were phase locked to each other, preventing relative drifts between them. In this measurement one can see, that the peak at 50 s to 60 s became much sharper, making the re-tuning of the microwave source the most likely source for this. More importantly however, one can see that the noise for long averaging times reduced significantly, now reaching stabilities of 300 ppb. It appears, that both the stability of the reference in the SynthHD as well as the quality of the temperature noise suppression are limiting for long averaging times.

All in all, I have shown in this chapter, that magnetic field stabilization using NV centers is a useful option if large magnetic field values need to be reached, especially if good DC stability is required.

The AC performance is mainly limited by the white noise floor in the error signal, leading to a stability of 1.1 mG being measured. If the white noise floor of the sample not in the feedback loop is removed, we are left with about 950 μG of magnetic field noise, giving an upper bound for the magnetic field noise actually present. In order to improve these values, more fluorescence would need to be evaluated, making the use of a different autobalanced photodetector necessary.

The DC performance seems to be - after locking the microwave sources to a stable reference - limited by remaining temperature noise. This noise might further decrease in the fiberized setup, when the sample is heatsunk to a silicon disk, due to the higher heat conductivity of silicon compared to sapphire glass. However, this might not be necessary: For 30 minutes averaging time we reach 300 ppb stability, but even the RMS noise over a whole day is only 157 μG, measured over a 1 Hz bandwidth.

6 Outlook

In this thesis I have demonstrated a magnetic field stabilization based on NV centers. Over the control loop's bandwidth of 1 kHz, stabilities of 1.1 mG were measured, although the main benefit of this method lies in its good DC stability, leading to fluctuations of only 157 μG over a 24 hour period, measured on a 1 Hz bandwidth.

In order to improve the noise floor of the magnetic field sensor, big changes in the setup would be necessary: The main limitation currently is the autobalanced photodetector, preventing us from using more fluorescence for the readout than we currently are, because the electronics in the feedback loop saturate. Otherwise, using higher laser powers and collecting more fluorescence would further improve stability, as we currently are not near optical power broadening or saturation of the optical transition.

The RedPitaya used for processing the data is not limiting accuracy right now - even for the best measurements, the input signal noise floor was about a factor 10 above the RedPitaya's noise floor. In case this limit is reached, one could possibly get another 10 dB of resolution by switching to the 16 bit version of the RedPitaya, and should obtain an extra 3 dB by digitizing the photodetector output using both its ADCs.

Also not limiting is the microwave setup - as we are close to power broadening, higher microwave powers would not improve the signal to noise ratio any more. For the currently realized noise floors, no spurs were observed. With an improved noise floor it might however be necessary to use two microwave amplifiers, and combine their outputs afterwards, to prevent higher order processes in the amplifier. Also, using a sample with narrower lines would increase contrast in the magnetic field reading.

With the described changes in the setup, a reduction of the noise floor by a factor 10 might be possible. On the other hand, with more elaborate, pulsed readout schemes, precisions in the $\frac{nG}{\sqrt{Hz}}$ range have been realized [27]. Problematic might be, that this would require new techniques for temperature noise suppression to be developed.

6.1 Integration into an atomic physics experiment

In the previous chapters I showed, that NV centers can be used as a sensor for stabilizing magnetic fields, with its main benefit being its ability to measure large fields. However, our main interest lies in using the sensor for stabilizing the field that the atoms in our experiments experience - this means that the sensor needs to be as close as possible to the atoms.

Recalling equation 3.3, this is problematic, because the space around the vacuum chamber in cold atom experiments is very limited. What we would like is the NV centers, and not the optical setup used for readout, to be close to the atoms. Because of the conservation of etendue, the fluorescence cannot be transported efficiently through free space, especially at long distances.

In order to use NV centers for sensing the magnetic field in remote locations, they are commonly glued to optical fibers, with the excitation laser being sent through the fiber, and the fluorescence coupled back into the optical fiber being evaluated [44, 45]. However, this collection is quite inefficient, because only the fluorescence emitted below the fiber's critical angle can be coupled back into the fiber.

For nanodiamonds, or diamonds containing single NV centers, the collection efficiency can be increased significantly by using imaging optics, e.g. GRIN lenses [46] or concave mirrors [47]. This works, because the NV centers are much smaller than the fiber and other optical elements, and can be considered a point source for that matter.

This is definetly not the case for the samples that we are using - our diamonds are about 1 mm in diameter, which is larger than common multi-mode fibers. To still couple in fluorescence under a solid angle of 2π, we need to either increase the fiber's critical angle, or its diameter. Increasing the critical angle of a fiber close to 90° is impractical, but the diameter can be increased by using a liquid light guide.

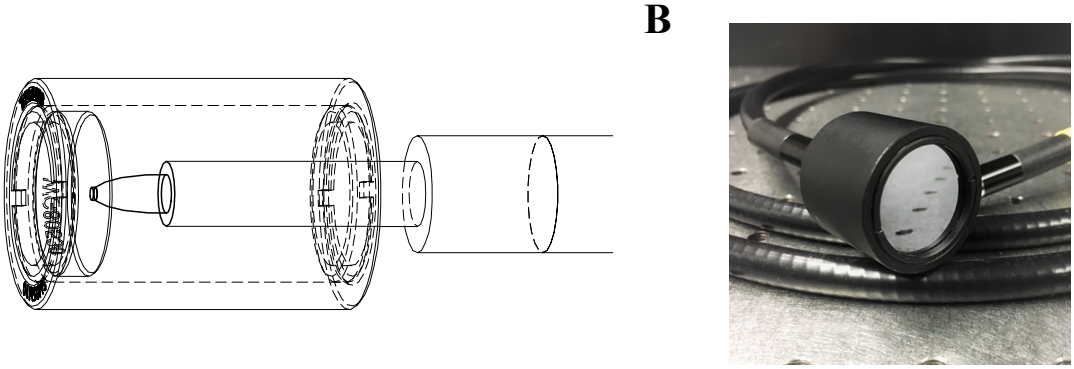

Figure 6.1: (A) Assembly of the diamond sample on top of a CPC, which couples the fluorescence into a liquid light guide. The diamond is heatsunk to a silicon disk, and the whole assembly is housed in an SM05 lenstube. **(B)** Photograph of the prototype tested.

To couple the fluorescence of the sample into the light guide (and concentrate the excitation light of the light guide onto the diamond) a compound parabolic concentrator can be used again. A test setup, using a CPC from Edmund optics, and a ∅5 mm liquid light guide, suffered from relatively low fluorescence collection efficiency in comparison to the free space setups, with about 15 times less fluorescence being available at the same laser power.

The main contribution for this loss comes from the CPC used: As few off the shelf CPCs are available, a CPC with an output diameter of 2.5 mm on the narrow end was used. Assuming that this surface was illuminated evenly, less than $^1/_5$ of the excitation laser power actually hit the 1 mm diameter diamond sample.

The use of a custom made CPC, with an input diameter of 3 mm and an output diameter of 1 mm, leading to a collection angle of 30° if made from a material with refractive index $n = 1.5$, might therefore improve the fluorescence collection for this setup significantly, making the integration into an atomic physics experiment possible.

6.2 Bringing NV centers into atomic physics

In this thesis I have built and characterized a magnetic field stabilization based on NV centers as a sensor - this might prove to be a useful tool in future experiments on ultracold quantum gases. One could now also go a step further, and ask the question whether the use of NV centers can solve more problems in atomic physics.

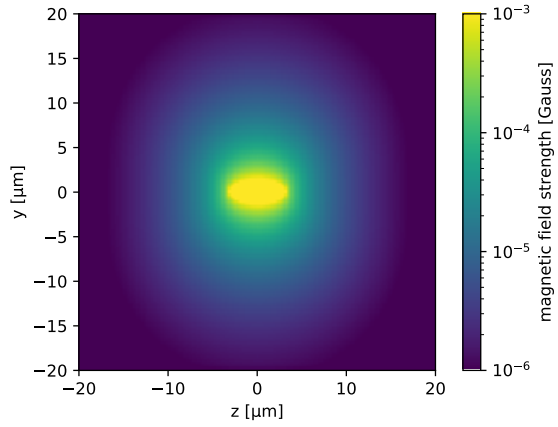

Figure 6.2: Magnetic field around a spin polarized pancake shaped cloud of 300000 rubidium atoms.

In figure 6.2 the magnetic field generated by a fully spin polarized cloud of 300000 rubidium atoms is shown. At first it looks like this magnetic field should be easily detectable with our NV center sensor. The problem here is, that our sensor size is on the order of mm, which means that only few of the defects would be at a μm distance to the atoms. This reduces the measurement precision significantly, and makes the diamond samples used in this thesis unsuitable for this task.

The production of a sample with preferred NV orientation using chemical vapour deposition [48, 49] onto a transparent material might however yield a sensor optimal for this task. Using pulsed readout schemes, much higher magnetic field sensitivities than that demonstrated

in this thesis can be realized [27]. This might potentially allow for reading out the cloud's spin state spatially resolved without destroying it, as would be the case e.g. with a Stern-Gerlach pulse.

The general readout scheme however could already be demonstrated with the diamond samples at hand: By placing them in a vapour cell containing a thermal gas, the spin state of the atoms nearby could be read out, even though only the NV centers on the sample's surface would contribute to this signal. Nevertheless, this might be a first step towards coupling NV centers to many-body states in ultracold quantum gases.

Appendix

A The Franck-Condon principle

The Franck-Condon principle [50] explains the shift of excitation transitions to higher energies, and the decay of excited states to lower energies.

Specifically in our case, the transition from the electronic ground state to the electronic excited state of an NV center requires higher energy photons than the fluorescence emitted the other way around. This is, because the excited state electron orbits are located at a larger distance to the defect.

As the excitation of the electron happens instantaneous compared to changes in the electron's spatial wavefunction, the transition to another state is much more likely to happen if there is an overlap between the two wavefunctions. This is not the case for the electronic excited vibrational gound state, as illustrated in figure A.1, making it necessary to deposit more energy, so that the electron can reach a higher lying phononic state, and the transition is driven efficiently.

Similarly, if the electronic excited state decays to the ground state, the best spatial overlap is given for higher lying vibrational levels, so that effectively less energy is emitted in the form of fluorescence.

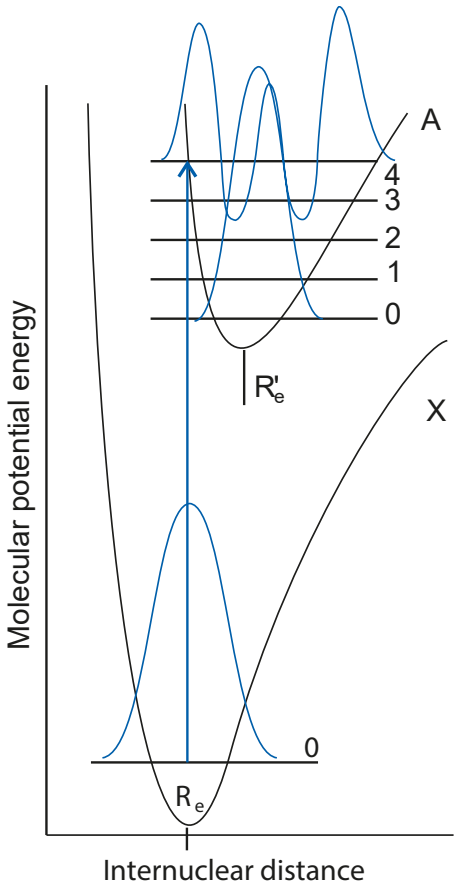

Figure A.1: Illustration of the Franck-Condon principle: Higher lying electronic states can only be reached, if additional energy is deposited. Taken from [50].

This is the reason why we can use a green laser to transfer the NV centers to the excited state, and use a long pass filter with a cut off with a wavelength higher than the zero phonon line - the wavelength, at which the transitions would happen, if no phonons were involved - to separate the fluorescence.

B Electronics

B.1 Current Controller board

When regulating the Current flowing through a coil pair the control bandwidth is often limited by the output capacity of the power supply and the inductance of the coil pair forming a resonance circuit. For the coil pairs and the power supply (a Delta Elektronika SM 18-50, with the high speed programming option) used in this thesis an, a resonance appeared at a few hundred Hz. This makes regulating away noise sources like higher harmonics of the 50 Hz noise hard, and introduces much additional noise near the resonance frequency.

To increase the control loop's bandwidth for a given coil geometry, one needs to reduce the output capacity of the power supply. Power supplies optimized for inductive loads are available from several manufacturers, but, especially for low current applications, a single transistor - e.g. a Darlington transistor - has a sufficiently low output capacity to be used to regulate the current.

The circuit used to regulate the current through the fast coil pair during this thesis is shown in figure B.1, and is based on a design by Helmut Strobel:

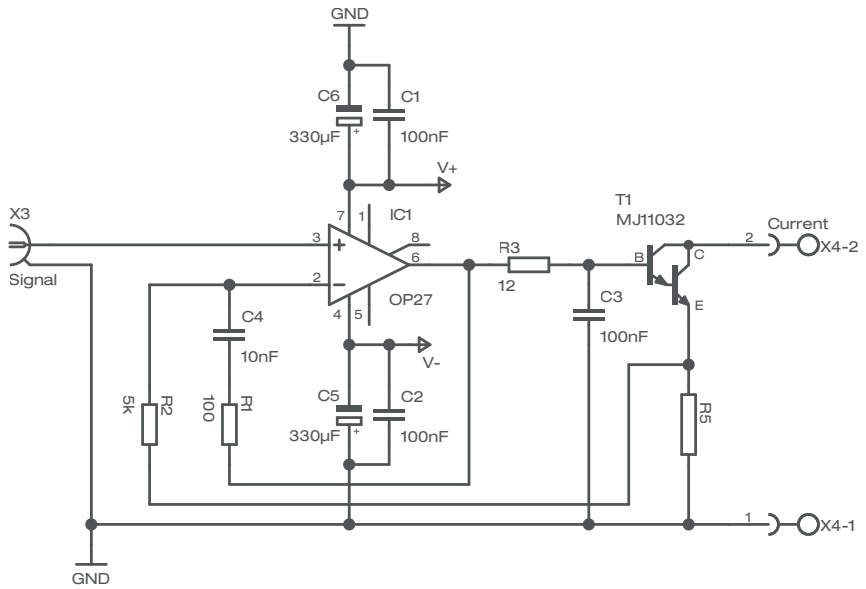

Figure B.1: Schematic of the circuit use to regulate the current through the fast coil pair.

The current control signal is fed into an OP27 op amp, which supplies the base current to a MJ11032 Darlington transistor. The transistor regulates the current through the coil pair on the low side, so the coils are connected to the power supply on one end, and to the collector of the Darlington on other. The current then flows through a high power resistor R5 (e.g. $1\,\Omega$) acting as a shunt resistor, which is then connected to ground / the low side of the power supply.

The voltage dropped across the shunt resistor is proportional to the current flowing through it, so feeding it back to the OP27 will regulate this voltage to be equal to the current control voltage - for R5 being $1\,\Omega$ this yields an output of $1\,\frac{\mathrm{A}}{\mathrm{V}}$.

In this circuit R3 and C3 act as a low pass, limiting the bandwidth of the current controller. For stability, R1 and C4 have to be used, limiting the opamp's gain at high frequencies, and preventing oscillation.

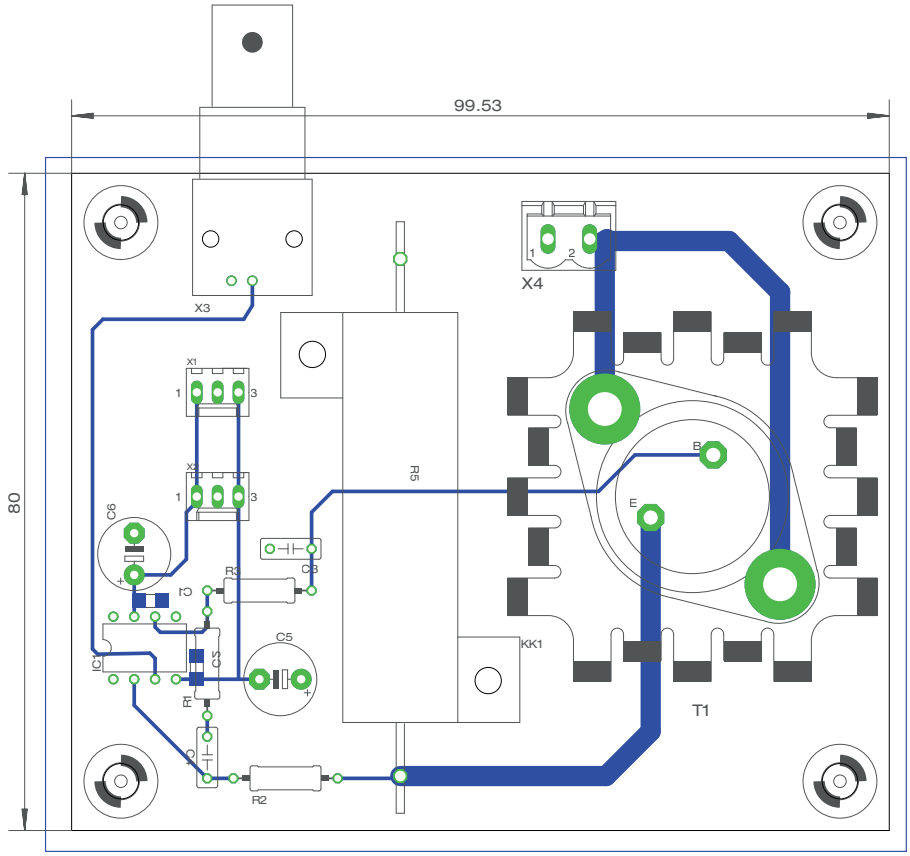

Figure B.2: Layout for the current controller board. The ground plane is not shown for clarity.

In figure B.2 the board layout for the circuit is shown: Wide traces in the current carrying section, a high power shunt resistor as well as a heatsink on the Darlington allow the board to regulate up to 10 A of current. Power for the opamp is supplied via a three-pin Molex connector, and a second connector allows for daisy chaining several boards together.

B.2 Modifications of PyRPL's FPGA source code

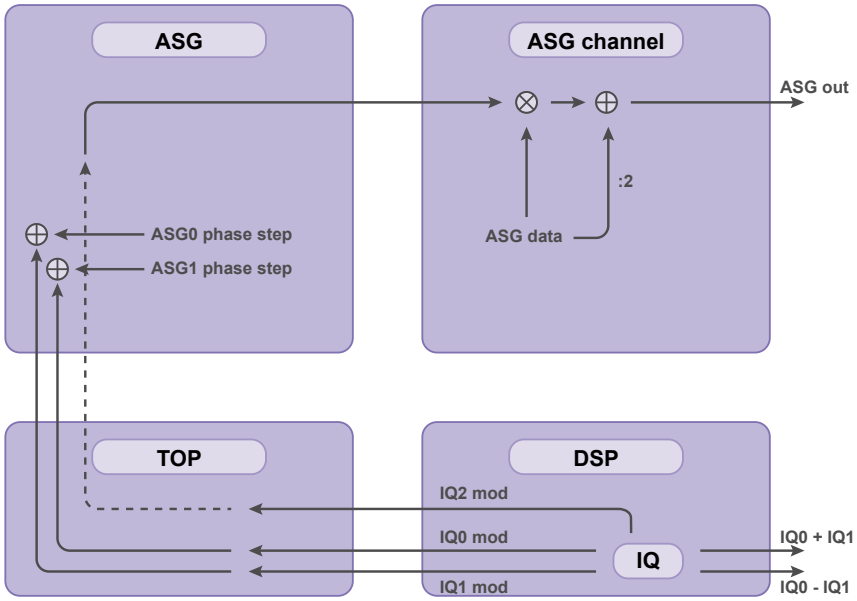

Figure B.3: Schematic of the modifications done on PyRPL's FPGA in order to control the NV center magnetic field stabilization on a RedPitaya.

A good point to start for understanding the modifications done to PyRPL's [34] FPGA is the DSP module: Here, the outputs of IQ module 0 and 1 are added and subtracted from each other, and outputted afterwards. For this the outputs of IQ module 2 were removed - the output IQ2 now outputs IQ0 - IQ1, and the output IQ2_2 outputs IQ0 + IQ1. These outputs contain the temperature drift compensated magnetic field signal, as well as the temperature shift signal used for re-tuning the microwave sources later on.

In addition to that, the modulation outputs of the three IQ modules are grabbed and passed through the top module. The modulation output of IQ0 and IQ1 are used in the ASG module to frequency modulate both AWGs for the lock in scheme. For this, the sinusoidal output of the IQ modules is added to the phase step, that each AWG takes every clock cycle, and that sets the frequency of the AWG.

The modulation of IQ2 is sent to the ASG channel modules, where it is multiplied with the (now already frequency modulated output) of the AWG to create the sidebands for addressing the NV center hyperfine states. This creates two sidebands at frequencies $f_{AWG} - f_{IQ2}$ and $f_{AWG} + f_{IQ2}$, but removes the original signal at f_{AWG}. Thus it is simply added back onto the signal, after being divided by 2 / shifted by one bit to give all three bands the same amplitude.

The modified source code as well as a bitstream file containing the compiled FPGA are available in a GitHub repository [51].

C Bibliography

[1] Fred Jendrzejewski. Short notes on the kondo effect and its potential realization in ultracold atomic gases. https://www.authorea.com/users/143341/articles/203821.

[2] V Kasper, F Hebenstreit, F Jendrzejewski, M K Oberthaler, and J Berges. Implementing quantum electrodynamics with ultracold atomic systems. *New Journal of Physics*, 19(2):023030, feb 2017.

[3] Alexander Mil, Torsten V. Zache, Apoorva Hegde, Andy Xia, Rohit P. Bhatt, Markus K. Oberthaler, Philipp Hauke, Jürgen Berges, and Fred Jendrzejewski. Realizing a scalable building block of a u(1) gauge theory with cold atomic mixtures. arXiv:1909.07641, https://arxiv.org/abs/1909.07641, 2019.

[4] V. Kasper, F. Hebenstreit, M.K. Oberthaler, and J. Berges. Schwinger pair production with ultracold atoms. *Physics Letters B*, 760:742 – 746, 2016.

[5] I.V. Hertel and C.P. Schulz. *Atoms, Molecules and Optical Physics 1: Atoms and Spectroscopy*. Graduate Texts in Physics. Springer Berlin Heidelberg, 2014.

[6] Cheng Chin, Rudolf Grimm, Paul Julienne, and Eite Tiesinga. Feshbach resonances in ultracold gases. *Rev. Mod. Phys.*, 82:1225–1286, Apr 2010.

[7] F. H. Mies, E. Tiesinga, and P. S. Julienne. Manipulation of feshbach resonances in ultracold atomic collisions using time-dependent magnetic fields. *Phys. Rev. A*, 61:022721, Jan 2000.

[8] E. Hodby, S. T. Thompson, C. A. Regal, M. Greiner, A. C. Wilson, D. S. Jin, E. A. Cornell, and C. E. Wieman. Production efficiency of ultracold feshbach molecules in bosonic and fermionic systems. *Phys. Rev. Lett.*, 94:120402, Mar 2005.

[9] Selim Jochim, M. Bartenstein, Anais Altmeyer, G. Hendl, Stefan Riedl, C. W. Chin, J. Hecker Denschlag, and Rudolf Grimm. Bose-einstein condensation of molecules. *Science*, 302 5653:2101–3, 2003.

[10] Markus Greiner, Cindy A. Regal, and Deborah S. Jin. Emergence of a molecular bose-einstein condensate from a fermi gas. *Nature*, 426(6966):537–540, 2003.

[11] M. Bartenstein, A. Altmeyer, S. Riedl, S. Jochim, C. Chin, J. Hecker Denschlag, and R. Grimm. Collective excitations of a degenerate gas at the bec-bcs crossover. *Phys. Rev. Lett.*, 92:203201, May 2004.

[12] T. Bourdel, L. Khaykovich, J. Cubizolles, J. Zhang, F. Chevy, M. Teichmann, L. Tarruell, S. J. J. M. F. Kokkelmans, and C. Salomon. Experimental study of the bec-bcs crossover region in lithium 6. *Phys. Rev. Lett.*, 93:050401, Jul 2004.

[13] G. B. Partridge, K. E. Strecker, R. I. Kamar, M. W. Jack, and R. G. Hulet. Molecular probe of pairing in the bec-bcs crossover. *Phys. Rev. Lett.*, 95:020404, Jul 2005.

[14] Simon L. Cornish, Sarah T. Thompson, and Carl E. Wieman. Formation of bright matter-wave solitons during the collapse of attractive bose-einstein condensates. *Phys. Rev. Lett.*, 96:170401, May 2006.

[15] Kevin E. Strecker, Guthrie B. Partridge, Andrew G. Truscott, and Randall G. Hulet. Formation and propagation of matter-wave soliton trains. *Nature*, 417(6885):150–153, 2002.

[16] C. R. Cabrera, L. Tanzi, J. Sanz, B. Naylor, P. Thomas, P. Cheiney, and L. Tarruell. Quantum liquid droplets in a mixture of bose-einstein condensates. *Science*, 359(6373):301–304, 2018.

[17] Igor Ferrier-Barbut, Holger Kadau, Matthias Schmitt, Matthias Wenzel, and Tilman Pfau. Observation of quantum droplets in a strongly dipolar bose gas. *Phys. Rev. Lett.*, 116:215301, May 2016.

[18] C. Gross, H. Strobel, E. Nicklas, T. Zibold, N. Bar-Gill, G. Kurizki, and M. K. Oberthaler. Atomic homodyne detection of continuous-variable entangled twin-atom states. *Nature*, 480(7376):219–223, 2011.

[19] Arno Trautmann. *Spin Dynamics and Feshbach Resonances in Ultracold Sodium-Lithium Mixtures*. PhD thesis, Heidelberg University, 7 2016.

[20] Christian Gross. *Spin squeezing and non-linear atom interferometrywith Bose-Einstein condensates*. PhD thesis, Heidelberg University, 2 2010.

[21] Pavel Ripka. Review of fluxgate sensors. *Sensors and Actuators A: Physical*, 33(3):129 – 141, 1992.

[22] R. S. Popovic. High resolution hall magnetic sensors. *2014 29th International Conference on Microelectronics Proceedings - MIEL 2014*, pages 69–74, 2014.

[23] Franz Baudenbacher, Luis Fong de los Santos, Jenny Holzer, and M. Radparvar. Monolithic low-transition-temperature superconducting magnetometers for high resolution imaging magnetic fields of room temperature samples. *Applied Physics Letters - APPL PHYS LETT*, 82, 05 2003.

[24] D. Drung, C. Abmann, J. Beyer, A. Kirste, M. Peters, F. Ruede, and T. Schurig. Highly sensitive and easy-to-use squid sensors. *IEEE Transactions on Applied Superconductivity*, 17(2):699–704, June 2007.

[25] Vito Giovanni Lucivero, Pawel Anielski, Wojciech Gawlik, and Morgan W. Mitchell. Shot-noise-limited magnetometer with sub-picotesla sensitivity at room temperature. *Review of Scientific Instruments*, 85(11):113108, 2014.

[26] W. Muessel, H. Strobel, D. Linnemann, D. B. Hume, and M. K. Oberthaler. Scalable spin squeezing for quantum-enhanced magnetometry with bose-einstein condensates. *Phys. Rev. Lett.*, 113:103004, Sep 2014.

[27] Thomas Wolf, Philipp Neumann, Kazuo Nakamura, Hitoshi Sumiya, Takeshi Ohshima, Junichi Isoya, and Jörg Wrachtrup. Subpicotesla diamond magnetometry. *Phys. Rev. X*, 5:041001, Oct 2015.

[28] D. Le Sage, K. Arai, D. R. Glenn, S. J. DeVience, L. M. Pham, L. Rahn-Lee, M. D. Lukin, A. Yacoby, A. Komeili, and R. L. Walsworth. Optical magnetic imaging of living cells. *Nature*, 496(7446):486–489, April 2013.

[29] Amila Ariyaratne, Dolev Bluvstein, Bryan A. Myers, and Ania C. Bleszynski Jayich. Nanoscale electrical conductivity imaging using a nitrogen-vacancy center in diamond. *Nature Communications*, 9(1), June 2018.

[30] Pengfei Wang, Sanyou Chen, Maosen Guo, Shijie Peng, Mengqi Wang, Ming Chen, Wenchao Ma, Rui Zhang, Jihu Su, Xing Rong, Fazhan Shi, Tao Xu, and Jiangfeng Du. Nanoscale magnetic imaging of ferritins in a single cell. *Science Advances*, 5(4), 2019.

[31] Marcus W. Doherty, Neil B. Manson, Paul Delaney, Fedor Jelezko, Jörg Wrachtrup, and Lloyd C.L. Hollenberg. The nitrogen-vacancy colour centre in diamond. *Physics Reports*, 528(1):1 – 45, 2013. The nitrogen-vacancy colour centre in diamond.

[32] P Maurer, Georg Kucsko, C Latta, Liang Jiang, Norman Yao, S Bennett, F Pastawski, David Hunger, N Chisholm, M. Markham, Daniel Twitchen, J. Cirac, and M Lukin. Room-temperature quantum bit memory exceeding one second. *Science (New York, N.Y.)*, 336:1283–6, 06 2012.

[33] Jörg Wrachtrup and Fedor Jelezko. Processing quantum information in diamond. *Journal of Physics: Condensed Matter*, 18(21):S807–S824, may 2006.

[34] L. Neuhaus, R. Metzdorff, S. Chua, T. Jacqmin, T. Briant, A. Heidmann, P. . Cohadon, and S. Deléglise. Pyrpl (python red pitaya lockbox) — an open-source software package for fpga-controlled quantum optics experiments. In *2017 Conference on Lasers and Electro-Optics Europe European Quantum Electronics Conference (CLEO/Europe-EQEC)*, pages 1–1, June 2017.

[35] Philip C. D. Hobbs. Noise cancelling circuitry for optical systems with signal dividing and combining means, 7 1992. US Patent 5,134,276.

[36] Philip C. D. Hobbs. *Building Electro-Optical Systems*. Wiley, 2009.

[37] Roland Winston, Lun Jiang, and Melissa Ricketts. Nonimaging optics: a tutorial. *Adv. Opt. Photon.*, 10(2):484–511, Jun 2018.

[38] Roland Winston, Lun Jiang, and Melissa Ricketts. Nonimaging optics: a tutorial. *Adv. Opt. Photon.*, 10(2):484–511, Jun 2018.

[39] J. Chaves. *Introduction to Nonimaging Optics, Second Edition*. CRC Press, 01 2017.

[40] M. W. Doherty, V. M. Acosta, A. Jarmola, M. S. J. Barson, N. B. Manson, D. Budker, and L. C. L. Hollenberg. Temperature shifts of the resonances of the nv^- center in diamond. *Phys. Rev. B*, 90:041201, Jul 2014.

[41] O. Chubar, P. Elleaume, and J. Chavanne. A 3d magnetostatics computer code for insertion devices. In *SRI97 Conference August 1997, J. Synchrotron Rad. 5, 481-484*, 1998.

[42] Albert Ryou and Jonathan Simon. Active cancellation of acoustical resonances with an fpga fir filter. *Review of Scientific Instruments*, 88(1):013101, 2017.

[43] WJ Riley. Handbook of frequency stability analysis. *NIST*, 1065:1–123, 01 2007.

[44] I. V. Fedotov, L. V. Doronina-Amitonova, D. A. Sidorov-Biryukov, N. A. Safronov, S. Blakley, A. O. Levchenko, S. A. Zibrov, A. B. Fedotov, S. Ya. Kilin, M. O. Scully, V. L. Velichansky, and A. M. Zheltikov. Fiber-optic magnetic-field imaging. *Opt. Lett.*, 39(24):6954–6957, Dec 2014.

[45] S. M. Blakley, I. V. Fedotov, S. Ya. Kilin, and A. M. Zheltikov. Room-temperature magnetic gradiometry with fiber-coupled nitrogen-vacancy centers in diamond. *Opt. Lett.*, 40(16):3727–3730, Aug 2015.

[46] Tim Schröder, Philip Engel, Eberhard Schmidt, and Oliver Benson. Integrated and compact fiber-coupled single-photon system based on nitrogen-vacancy centers and gradient-index lenses. *Opt. Lett.*, 37(14):2901–2903, Jul 2012.

[47] Dewen Duan, Vinaya Kumar Kavatamane, Sri Ranjini Arumugam, Ganesh Rahane, Yan-Kai Tzeng, Huan-Cheng Chang, Hitoshi Sumiya, Shinobu Onoda, Junichi Isoya, and Gopalakrishnan Balasubramanian. Enhancing fluorescence excitation and collection from the nitrogen-vacancy center in diamond through a micro-concave mirror. *Applied Physics Letters*, 113(4):041107, 2018.

[48] Christian Osterkamp, Martin Mangold, Johannes Lang, Priyadharshini Balasubramanian, Tokuyuki Teraji, Boris Naydenov, and Fedor Jelezko. Engineering preferentially-aligned nitrogen-vacancy centre ensembles in cvd grown diamond. *Scientific Reports*, 9(1):5786, 2019.

[49] Hayato Ozawa, Kosuke Tahara, Hitoshi Ishiwata, Mutsuko Hatano, and Takayuki Iwasaki. Formation of perfectly aligned nitrogen-vacancy-center ensembles in chemical-vapor-deposition-grown diamond (111). *Applied Physics Express*, 10(4):045501, mar 2017.

[50] P.W. Atkins and R.S. Friedman. *Molecular Quantum Mechanics*. OUP Oxford, 2011.

[51] Alexander Hesse. Pyrpl-modification. Github repository, https://github.com/ahesse93/PyRPL-Modification, 2019.

Acknowledgments

- First and foremost I would like to thank Fred, for being such a helpful supervisor, and for trusting me with so much freedom working on this thesis. I first started working with him for my Bachelor's thesis three and a half years ago, and I've been learning from him ever since.
- I would also like to thank Selim, for being the second corrector of this thesis, and for his advice on low-cost lasers.
- Of course, all my thanks also go to the whole Matterwave team, for all the breakfasts shared, barbecues enjoyed and and running dinners survived. It was great fun working with you for the last years!
- Every group has one person, that everybody asks for advice if the experiment does not behave as wanted. For us, this is clearly Helmut, and without the many times he magically made RF components appear and problems disappear this thesis would probably still be in its beginnings. Thank you for all your help and advice!
- Special thanks also goes to all the coffee (or tea) drinking people gathering in the BECK office every day after lunch! You made the post-lunch-coma so much more enjoyable! Very special thanks also go to clever Max, for proofreading parts of this thesis, and to Lisa, for proofreading everything else that had to be proofread!
- Thank you also to Jörg Wrachtrup and his team in Stuttgart, especially Jakob, Julia and Durga, for trusting us with their diamonds, and helping us set up this experiment!
- A big thank you also goes to all my friends, the trivia on Thursdays team, and of course my family for all the support, and for keeping me busy outside the lab!

Erklärung:

Ich versichere, dass ich diese Arbeit selbstständig verfasst habe und keine anderen als die angegebenen Quellen und Hilfsmittel benutzt habe.

Heidelberg, den 18.11.2019 .....